Simulating Dynamical Phases of Chiral $p + ip$ Superconductors with a Trapped ion Magnet

Athreya Shankar,[1,2,*] Emil A. Yuzbashyan,[3] Victor Gurarie,[4,5] Peter Zoller,[1,2] John J. Bollinger,[6] and Ana Maria Rey[5,7,†]

[1] *Institute for Theoretical Physics, University of Innsbruck, Innsbruck, Austria*
[2] *Institute for Quantum Optics and Quantum Information of the Austrian Academy of Sciences, Innsbruck, Austria*
[3] *Center for Materials Theory, Rutgers University, Piscataway, New Jersey 08854, USA*
[4] *Department of Physics, University of Colorado, Boulder, Colorado 80309, USA*
[5] *Center for Theory of Quantum Matter, University of Colorado, Boulder, Colorado 80309, USA*
[6] *National Institute of Standards and Technology, Boulder, Colorado 80309, USA*
[7] *JILA, National Institute of Standards and Technology,and Department of Physics, University of Colorado, Boulder, Colorado, 80309, USA*

(Received 21 April 2022; revised 16 September 2022; accepted 31 October 2022; published 30 November 2022)

Two-dimensional $p + ip$ superconductors and superfluids are systems that feature chiral behavior emerging from the Cooper pairing of electrons or neutral fermionic atoms with nonzero angular momentum. Their realization has been a longstanding goal because they offer great potential utility for quantum computation and memory. However, they have so far eluded experimental observation both in solid-state systems as well as in ultracold quantum gases. Here, we propose to leverage the tremendous control offered by rotating two-dimensional trapped-ion crystals in a Penning trap to simulate the dynamical phases of two-dimensional $p + ip$ superfluids. This is accomplished by mapping the presence or absence of a Cooper pair into an effective spin-1/2 system encoded in the ions' electronic levels. We show how to infer the topological properties of the dynamical phases, and discuss the role of beyond mean-field corrections. More broadly, our work opens the door to use trapped-ion systems to explore exotic models of topological superconductivity and also paves the way to generate and manipulate skyrmionic spin textures in these platforms.

DOI: 10.1103/PRXQuantum.3.040324

I. INTRODUCTION

The observation and classification of dynamical behaviors in quantum many-body systems constitute a core milestone in quantum science. One fascinating and promising paradigm comprises the dynamical phases predicted to emerge from quenches of superconductors and superfluids [1–3], systems that feature Cooper pairing of electrons or neutral fermionic atoms. In particular, topological $p + ip$ Bardeen-Cooper-Schrieffer (BCS) superconductors (in charged electrons) or superfluids (in neutral atoms)—systems that feature nontrivial topological properties [4] and gapless, chiral edge states that circulate around the boundary—are especially exciting given their potential use for topological quantum computation.

Despite intensive theoretical efforts, $p + ip$ superfluids have eluded experimental observation, with the only confirmed realization being the A phase of ^{3}He, which ironically is one of the oldest-known superfluids but is also hard to control and manipulate. The realization of $p + ip$ superfluids in ultracold fermionic quantum gases, which are currently the leading platform for quantum simulation of correlated matter, has also proved to be difficult. The reason is that, in spite of all the attractive features of ultracold quantum gases, the control and manipulation of p-wave interactions in these systems has remained a challenge since p-wave interactions are weak under standard conditions and require Feshbach resonances to enhance them. The latter unfortunately introduce strong three-body processes that make the gas unstable and destroy the desired pairing processes [5–8], although schemes circumventing this problem have been proposed [9–11]. Theory proposals have also suggested the observation of topological superfluids by suddenly bringing weakly interacting atoms close

*athreyas@iisc.ac.in
†arey@jilau1.colorado.edu

to a Feshbach resonance [12], but to date experimental efforts remain unsuccessful.

In the present work, we propose a pathway towards the observation of nonequilibrium dynamical phases of topological $p + ip$ superfluids by using a two-dimensional (2D) crystal of ions in a Penning trap. This platform offers a high degree of control and flexibility in state initialization, interaction control, and readout that have been previously leveraged for the sensing of weak electric fields and for the simulation of quantum magnets [13,14]. In this system, we propose to encode a spin-1/2 degree of freedom in two electronic states of the ions, which, via the Anderson pseudospin mapping [15], are used to simulate the presence or the absence of a Cooper pair. A crucial advantage of this approach is that the fermionic degrees of freedom are encoded in a synthetic internal dimension (electronic levels) that can be cooled down to a zero temperature, pure state via optical pumping. This is in striking contrast to actual fermionic systems where motional degrees of freedom are hard to cool down.

Our proposal takes advantage of the fact that the ion crystal in a Penning trap is rotating in the lab frame [16]. This feature has never before been exploited in the context of quantum simulation and, in fact, it is often viewed as an impediment, e.g., to perform single site addressing. We show that by tuning the orientation and parameters of the laser beams that are typically used to couple the electronic and motional degrees of freedom of the crystal, we can engineer controllable effective interactions that simulate the Hamiltonian of a $p + ip$ superfluid. Tuning the laser parameters also allows us to (i) prepare initial states that resemble the low-energy conditions of a p-wave superfluid, (ii) control the relative strength between the kinetic energy and pairing interaction terms in order to observe the three different mean-field dynamical phases predicted to exist in $p + ip$ superfluids [4], and (iii) measure a superconducting order parameter for classifying the dynamical phases. Moreover, since state-of-the-art ion crystals are not in the thermodynamic limit but are instead limited to $\lesssim 500$ ions, they naturally open a path to explore modifications to the nonequilibrium dynamics arising from beyond-mean-field effects.

A key appeal of $p + ip$ superfluids compared to ordinary superfluids is the possibility of featuring states with nontrivial topological order. In an ordinary superfluid or superconductor, the BCS and the BEC (Bose Einstein condensate) regimes—which respectively favor weakly bound Cooper pairs and a Bose-Einstein condensate of tightly bound molecules made of two fermions—are continuously connected and are only distinguished by the strength of the pairing. In contrast, the two regimes exhibit different topological behaviors in 2D $p + ip$ superfluids, with a genuine quantum phase transition separating the topologically nontrivial BCS phase from the topologically trivial BEC phase in the equilibrium situation. This feature extends into the nonequilibrium regime, where the dynamical phases exhibit a dynamical topological quantum phase transition [4]. Here, we show how to engineer both topologically trivial and nontrivial dynamical phases in our system and demonstrate how their topological character can be distinguished by inferring an appropriate winding number and additionally confirmed by measurements of the effective Cooper pair distribution function.

II. TWO-DIMENSIONAL $p + ip$ SUPERFLUIDS

We consider identical fermions in two dimensions, for which the Pauli exclusion principle forbids scattering in the s-wave channel. As a result, the next higher angular momentum channel, namely p-wave scattering ($l = 1$), dominates with $l > 1$ channels being negligible at low energies. The angular dependence of two-body p-wave interactions in two dimensions is $P_{l=1}(\cos\xi) = \cos\xi$, where the $P_l(x)$ are Legendre polynomials and ξ is the angle between the two-dimensional fermion momenta before ($\mathbf{q}$) and after ($\mathbf{p}$) collision in the center-of-mass frame. Furthermore, for a generic short-range potential, the interaction in the lth channel depends on the magnitude of the momenta on long scales as $p^l q^l$, where p and q are the magnitudes of $\mathbf{p}$ and $\mathbf{q}$. The above considerations imply that the simplest and most natural p-wave interactions between identical fermions in two dimensions are proportional to $\mathbf{p} \cdot \mathbf{q}$. Therefore, we arrive at the Hamiltonian

$$\hat{H} = \sum_{\mathbf{p}} \frac{p^2}{2m} \hat{c}^\dagger_{\mathbf{p}} \hat{c}_{\mathbf{p}} - \frac{\lambda}{2m} \sum_{\mathbf{k},\mathbf{p},\mathbf{q}} \mathbf{p} \cdot \mathbf{q} \hat{c}^\dagger_{\mathbf{k}/2+\mathbf{p}} \hat{c}^\dagger_{\mathbf{k}/2-\mathbf{p}} \hat{c}_{\mathbf{k}/2-\mathbf{q}} \hat{c}_{\mathbf{k}/2+\mathbf{q}}. \tag{1}$$

Here, m is the electron mass and $\hat{c}^\dagger_{\mathbf{p}}, \hat{c}_{\mathbf{p}}$ are fermionic creation and annihilation operators for a fermion with momentum $\mathbf{p}$. The first term describes the single-particle dispersion, i.e., the kinetic energy of fermions at different momenta $\mathbf{p}$. The second term has the form of attractive BCS p-wave interactions ($\lambda > 0$, dimensionless) [17]. Here, $\mathbf{k}$ denotes the center-of-mass momentum of a Cooper pair of fermions, while $\pm\mathbf{q}$ and $\pm\mathbf{p}$ respectively describe the momenta of these fermions in the center-of-mass frame before and after the collision.

In the theory of superconductivity, the low-energy physics is determined by Cooper pairs with zero center-of-mass momentum, which allows us to retain only the $\mathbf{k} = 0$ terms in Eq. (1), resulting in

$$\hat{H} = \sum_{\mathbf{p}} \frac{p^2}{2m} \hat{c}^\dagger_{\mathbf{p}} \hat{c}_{\mathbf{p}} - \frac{\lambda}{2m} \sum_{\mathbf{p},\mathbf{q}} \mathbf{p} \cdot \mathbf{q} \hat{c}^\dagger_{\mathbf{p}} \hat{c}^\dagger_{-\mathbf{p}} \hat{c}_{-\mathbf{q}} \hat{c}_{\mathbf{q}}. \tag{2}$$

This Hamiltonian assumes that Cooper pairs are only created and destroyed with zero center-of-mass momentum and neglects pair-breaking processes.

Under these conditions, the low-energy physics can be mapped on to the dynamics of a collection of interacting spin-1/2 systems via the Anderson pseudospin mapping [15] that introduces spin-1/2 operators at each momentum $\mathbf{p}$:

$$2\hat{s}^Z_{\mathbf{p}} = \hat{c}^\dagger_{\mathbf{p}}\hat{c}_{\mathbf{p}} + \hat{c}^\dagger_{-\mathbf{p}}\hat{c}_{-\mathbf{p}} - 1,$$
$$\hat{s}^+_{\mathbf{p}} = \hat{c}^\dagger_{\mathbf{p}}\hat{c}^\dagger_{-\mathbf{p}}, \qquad \hat{s}^-_{\mathbf{p}} = \hat{c}_{-\mathbf{p}}\hat{c}_{\mathbf{p}}. \tag{3}$$

Here, the presence or absence of a Cooper pair at momentum $\mathbf{p}$ corresponds to the eigenstates $|\uparrow\rangle_{\mathbf{p}}, |\downarrow\rangle_{\mathbf{p}}$ of $\hat{s}^Z_{\mathbf{p}}$ with eigenvalues $\pm 1/2$, respectively, and the raising and lowering operators $\hat{s}^\pm_{\mathbf{p}}$ describe the creation and annihilation of this Cooper pair. In terms of the Anderson pseudospin operators, Hamiltonian (2) can be expressed as [18]

$$\hat{H} = \sum_{\mathbf{p}} \frac{p^2}{m}\hat{s}^Z_{\mathbf{p}} - \frac{2\lambda}{m}\sum_{\mathbf{p},\mathbf{q}} \mathbf{p}\cdot\mathbf{q}\hat{s}^+_{\mathbf{p}}\hat{s}^-_{\mathbf{q}}. \tag{4}$$

Equation (4) describes an all-to-all interacting spin model. We note that although fermions interact via short-ranged interactions in real space, this spin model describes the p-wave interactions in momentum space, where the interactions are all to all, as described by Eq. (2).

The ground state of the spin model (4) is doubly degenerate: it is either a $p_x + ip_y$ or a $p_x - ip_y$ superfluid. It possesses the property that the spin orientation is correlated with the azimuthal angle $\phi_{\mathbf{p}}$ in momentum space, giving rise to chiral spin textures as depicted in Fig. 1(a).

The ground state breaks the $U(1)$ symmetry of Eq. (4) as all superconductors do and in this case it also breaks the time-reversal symmetry. A winding number Q can be ascribed to the spin texture, based on which the state can be classified as belonging to a topologically nontrivial BCS phase ($Q = 1$) or a topologically trivial BEC phase ($Q = 0$). Physically, assuming that spins at large momenta are always held fixed in $|\downarrow\rangle$, the spin texture is topologically nontrivial if the central spin at $\mathbf{p} = 0$ is in $|\uparrow\rangle$, whereas it is trivial if this spin is in $|\downarrow\rangle$.

The quench dynamics of $p + ip$ superconductors were theoretically studied [4] by considering a chiral variant of the spin model (4) given by

$$\hat{H} = \sum_{\mathbf{p}} \frac{p^2}{m}\hat{s}^Z_{\mathbf{p}} - \frac{\lambda}{m}\sum_{\mathbf{p},\mathbf{q}} pq e^{-i(\phi_{\mathbf{p}}-\phi_{\mathbf{q}})}\hat{s}^+_{\mathbf{p}}\hat{s}^-_{\mathbf{q}}, \tag{5}$$

where p and $\phi_{\mathbf{p}}$ are the magnitude and azimuthal angle for the 2D momentum $\mathbf{p}$. This Hamiltonian breaks time-reversal symmetry explicitly, and preferentially selects the $p_x - ip_y$ over $p_x + ip_y$ pairing, which are degenerate in the time-reversal-invariant Hamiltonian (4). The attractiveness of Eq. (5) is that, unlike the full Hamiltonian (4), the interaction is separable and belongs to the class of integrable pairing models that derive from Gaudin algebra [19], allowing for an analytical solution of the dynamical phases. Nevertheless, both Hamiltonians possess the same $p + ip$ ground state and dynamical phases in the thermodynamic limit [4]. In this work, we focus on the quantum simulation of the chiral model (5).

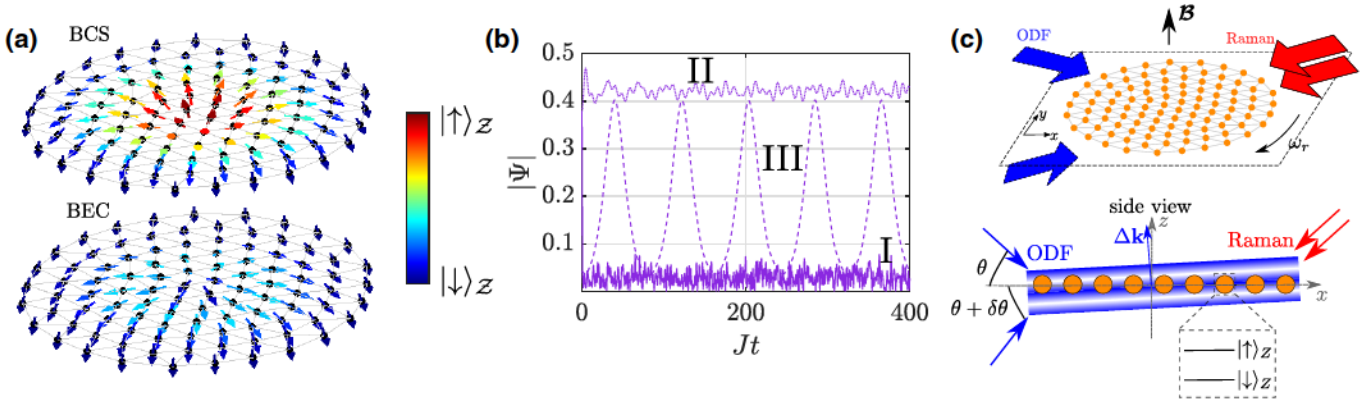

FIG. 1. Probing dynamical phases of $p + ip$ superfluids using ion crystals in Penning traps. (a) The fermionic model is mapped on to spins encoded in the internal states of the ions, where spin up (down) represents the presence (absence) of a Cooper pair (Anderson pseudospin mapping). Here we show representative spin textures that can be engineered for the topologically nontrivial BCS and trivial BEC phases. (b) The dynamical phases are classified according to the long-time behavior of the magnitude of an order parameter—phase I, $|\Psi(t)| \to 0$; phase II, $|\Psi(t)| \to$ nonzero constant; phase III, $|\Psi(t)|$ displays persistent oscillations. (c) Schematic of our experimental proposal. State initialization, p-wave interactions and readout are all achieved using appropriate parameters for a pair of optical dipole force (ODF) lasers and a pair of copropagating Raman lasers. In contrast to prior implementations, the ODF difference wave vector $\delta\mathbf{k}$ has both an out-of-plane and in-plane component (see side view). The result is a tilted traveling-wave lattice that crosses the crystal plane slightly obliquely and thus couples the ions' electronic degrees of freedom, the out-of-plane center-of-mass mode, and the in-plane crystal rotation. The spin-space directions $\mathcal{Z}$ in panel (a) and Z in panel (c) are related by a rotation, as discussed in Sec. III.

In the thermodynamic limit, where mean-field theory is exact, the dynamics can be pictured as each spin precessing about a local magnetic field:

$$\frac{d}{dt}\langle\hat{\mathbf{s}}_\mathbf{p}\rangle = \langle\hat{\mathbf{s}}_\mathbf{p}\rangle \times \mathbf{B}_\mathbf{p}. \tag{6}$$

Here, $\langle\hat{\mathbf{s}}_\mathbf{p}\rangle$ is the expectation value of the spin vector at momentum $\mathbf{p}$ and $\mathbf{B}_\mathbf{p}$ is the local magnetic field with components

$$\begin{aligned} B_\mathbf{p}^X &= -p\cos(\phi_\mathbf{p})\mathrm{Re}[\Psi] - p\sin(\phi_\mathbf{p})\mathrm{Im}[\Psi], \\ B_\mathbf{p}^Y &= p\cos(\phi_\mathbf{p})\mathrm{Im}[\Psi] - p\sin(\phi_\mathbf{p})\mathrm{Re}[\Psi], \\ B_\mathbf{p}^Z &= -\frac{p^2}{m}, \end{aligned} \tag{7}$$

written in terms of an order parameter Ψ given by

$$\Psi(t) = -\frac{2\lambda}{m}\sum_\mathbf{p} p e^{i\phi_\mathbf{p}}\langle\hat{s}_\mathbf{p}^-(t)\rangle. \tag{8}$$

Mean-field theory predicts the emergence of three dynamical phases when the system is initialized in its ground state and the pairing strength λ is quenched. They have been classified according to the long-time behavior of $|\Psi(t)|$ as illustrated in Fig. 1(b), where we plot a dimensionless and normalized version of the order parameter [see Eq. (13)]. In phase I, the single-particle kinetic energy term ($B_\mathbf{p}^Z$) dominates and $|\Psi(t)| \to 0$. In phases II and III interactions instead stabilize a finite order parameter. In phase II, $|\Psi(t)|$ tends to a nonzero constant value, while in phase III, also known as a self-generated Floquet phase [1], $|\Psi(t)|$ features persistent oscillations.

The topological properties of the dynamical phases are best understood in terms of a second winding number W, which can take on a nontrivial value of 1 in phases II and III. Although this quantity is formally defined in terms of retarded single-particle Green functions [4], it can be physically interpreted in phase II as the winding of the magnetic field texture in an appropriate rotating frame. In the thermodynamic limit, mean-field theory predicts that the long-time order parameter in phase II can be written as

$$\Psi(t) = \Psi_\infty e^{-2i\mu_\infty t}, \tag{9}$$

where Ψ_∞ is the magnitude in the limit $t \to \infty$ and μ_∞ is a dynamical chemical potential. In a frame rotating at $2\mu_\infty$, the spins precess under a static effective magnetic field $\overline{\mathbf{B}}_\mathbf{p}$ whose texture can be analogous to the spin texture in a $p + ip$ ground state. The winding number W is computed as

$$W = \frac{1}{4\pi}\int dp_x dp_y \hat{\overline{\mathbf{B}}}_\mathbf{p} \cdot \left(\frac{d\hat{\overline{\mathbf{B}}}_\mathbf{p}}{dp_x} \times \frac{d\hat{\overline{\mathbf{B}}}_\mathbf{p}}{dp_y}\right), \tag{10}$$

where $\hat{\overline{\mathbf{B}}}_\mathbf{p}$ denotes the corresponding unit vector in the rotating frame. In particular, the Z component of $\overline{\mathbf{B}}_\mathbf{p}$ is given by $\overline{B}_\mathbf{p}^Z = B_\mathbf{p}^Z + 2\mu_\infty\hat{\mathbf{e}}_Z$. While the spins at large momenta $p \to \infty$ experience a field $\overline{\mathbf{B}}_\mathbf{p} \approx -(p^2/m)\hat{\mathbf{e}}_Z$ that points down, the central spin at $\mathbf{p} = \mathbf{0}$ is isolated from the other spins and experiences an effective magnetic field $\overline{\mathbf{B}}_\mathbf{0} = 2\mu_\infty\hat{\mathbf{e}}_Z$. Therefore, the magnetic field texture is BCS-like and topologically nontrivial ($W = 1$) for $\mu_\infty > 0$ ($\overline{\mathbf{B}}_\mathbf{0}$ pointing up) while it is BEC-like and topologically trivial ($W = 0$) for $\mu_\infty < 0$ ($\overline{\mathbf{B}}_\mathbf{0}$ pointing down).

III. IMPLEMENTATION WITH PENNING TRAPS

We now discuss how the spin model (5) can be simulated with ion crystals in a Penning trap, where the pseudospin-1/2 system is encoded in two long-lived hyperfine states of each trapped ion. In this trap, ions self-organize into a planar crystal with an approximate triangular lattice structure under the influence of static trapping fields [20]. An electric quadrupole field $\boldsymbol{\mathcal{E}}$ accomplishes axial trapping and confines the ions to a single plane. The addition of a strong axial magnetic field $\boldsymbol{\mathcal{B}}$ leads to an $\boldsymbol{\mathcal{E}} \times \boldsymbol{\mathcal{B}}$ drift of the ions in this plane. This rotation provides radial confinement and the corresponding rotation frequency ω_r can be precisely controlled by additional electrodes. The out-of-plane motion of a crystal of N ions is described using N normal modes of vibration, called the drumhead modes. The highest frequency drumhead mode is the center-of-mass (c.m.) mode with frequency ω_1, which is well separated from the rest of the modes and hence can be well resolved [16].

In our modeling, the drumhead c.m. mode is treated quantum mechanically and described by bosonic creation and annihilation operators $\hat{a}_1^\dagger, \hat{a}_1$. On the other hand, the planar motion is dominated by the crystal rotation, and is hence treated classically with the x_j and y_j coordinates of ion j undergoing uniform circular motion at radius r_j from the trap center, with frequency ω_r and azimuthal phase offset ϕ_j.

As a first step to realize Hamiltonian (5), we engineer a Jaynes-Cummings-type interaction between each spin and the drumhead c.m. mode, with the coupling depending on the planar position of the ion as viewed in the crystal rotating frame. As we explain shortly, the Hamiltonian we engineer is given by

$$\begin{aligned} \hat{H}_{2\mathrm{ch}} = &\sum_{j=1}^N B_1 \tilde{r}_j^2 \hat{\mathfrak{s}}_j^\mathcal{Z} + \delta_1 \hat{a}_1^\dagger \hat{a}_1 \\ &- \sum_{j=1}^N \frac{G}{i\sqrt{N}}\tilde{r}_j\left(\hat{\mathfrak{s}}_j^- \hat{a}_1^\dagger e^{i\phi_j} - \hat{a}_1 \hat{\mathfrak{s}}_j^+ e^{-i\phi_j}\right). \end{aligned} \tag{11}$$

This Hamiltonian is written in a rotated spin space $\mathcal{Z} \equiv -X$, $\mathcal{X} \equiv Z$, $\mathcal{Y} \equiv Y$, and $\hat{\mathfrak{s}}_j$ denotes spin operators in this rotated space. Here, $\tilde{r}_j = r_j/R$ is the radial coordinate normalized to the crystal radius R, B_1 is a frequency controlling the dispersion of the spins, δ_1 is an effective

detuning of the c.m. mode from the spins, and G is a frequency controlling the spin-mode coupling strength. In particular, the amplitude and phase of the coupling of spin j to the c.m. mode respectively depend on $\tilde{r}_j$ and ϕ_j.

Equation (11) describes the Hamiltonian for the so-called two-channel model of a p-wave superconductor. The c.m. mode plays the role of the bosonic molecular channel, while each ion encodes an Anderson pseudospin in its electronic states. Here, spin up (down) indicates the presence (absence) of a Cooper pair. While the Anderson pseudospins live in a lattice in momentum space where the coordinates are (p_x, p_y), the role of momentum is instead played here by the position (x_j, y_j) of each ion j in the crystal plane. "Momentum"-dependent rates appear in the single-particle and interaction terms through the radius r_j and the phase factors $e^{\pm i\phi_j}$.

Subsequently, an effective spin model can be derived in the situation when $\delta_1 \gg G, B_1$. Using effective Hamiltonian theory [21] and assuming that the c.m. mode is in the motional ground state, we obtain the one-channel model given by

$$\hat{H}_{1\mathrm{ch}} = K \sum_j \tilde{r}_j^2 \hat{\mathfrak{s}}_j^Z - \frac{J}{N} \sum_{j \neq k} \tilde{r}_j \tilde{r}_k \hat{\mathfrak{s}}_j^+ \hat{\mathfrak{s}}_k^- e^{-i(\phi_j - \phi_k)}, \quad (12)$$

where $J = G^2/\delta_1$ and $K = B_1 - J/N$. Equation (12) is essentially the one-channel p-wave Hamiltonian (5) that we wish to simulate. The ratio K/J is a measure of the inverse interaction strength ($\sim 1/\lambda$) since it quantifies the relative importance of the kinetic energy and interaction terms.

We now briefly outline how Hamiltonian (11) can be engineered while presenting the detailed derivation in Appendix A. Coupling between the spins and the crystal motion is enabled by the application of an optical dipole force (ODF) that gives rise to spatially dependent ac Stark shifts on the spin states [22]. The ODF is generated by two traveling-wave lasers with difference wave vector $\Delta\mathbf{k}$ and beatnote frequency μ_r. In typical applications, only the axial motion is coupled to the spin and hence $\Delta\mathbf{k} \parallel \hat{\mathbf{e}}_z$ [13,14]. However, in this work, we consider the $\Delta\mathbf{k}$ to have nonzero components both along the $\hat{\mathbf{e}}_z$ and $\hat{\mathbf{e}}_x$ directions [Fig. 1(c)]. The result is a spatially varying ac Stark shift that depends on both the in-plane and out-of-plane motions of the ions, thereby coupling the spins to the motion along both the directions. The spin-motion coupling strength G in Eq. (11) can be controlled by the intensity of the ODF beams and the effective Lamb-Dicke parameters that govern the coupling to the out-of-plane and in-plane motions, as explained in Appendix A.

A second ingredient in our proposal consists of a pair of copropagating Raman lasers that drives spin flips without coupling to the motion. We assume that the two Raman lasers have an identical but tunable beam waist w, leading to an effective two-photon Rabi frequency that is radially varying as $B(r) = B_0 e^{-r^2/w^2}$ and corresponding Hamiltonian $\hat{H}_{\mathrm{Raman},j} = B(r_j)\hat{s}_j^X$. For $w \gg R$, where R is the crystal radius, we can approximate $B(r) \approx B_0 - B_0 r^2/w^2$.

The role of the Raman drive is twofold and becomes apparent in the rotated spin space (see Appendix A). First, the spatially homogeneous drive with strength B_0 serves to break the symmetry between a Jaynes-Cummings and an anti-Jaynes-Cummings-type interaction of the spins and the drumhead c.m. mode that arise due to the ODF. The Jaynes-Cummings term can then be selectively brought near resonance by tuning the ODF beatnote frequency to be $\mu_r = B_0 + \omega_1 + \omega_r - \delta_1$, where δ_1 is the effective detuning that appears in Eq. (11). The frequency μ_r is tuned close to $\omega_1 + \omega_r$ ($\delta_1, B_0 \ll \omega_1, \omega_r$; see Appendix B) and not simply ω_1 in order to enhance the simultaneous coupling to the c.m. mode and the planar rotation that is enabled by the tilted ODF beams. Second, the beam waist w serves as a control knob for tuning the single-particle dispersion, i.e., $B_1 = B_0 R^2/w^2$. We note that the Raman beams can be replaced with a microwave drive that limits the tunability of B_1 but allows for a simpler implementation and reduced decoherence (see Appendix B). The ability to control G, δ_1 and B_1 in turn enables us to tune the ratio K/J in the one-channel model.

We present potential experimental parameters for realizing our proposal in Appendix B and study the adverse impact of off-resonant terms in Appendices C and D. Our study suggests that, in current traps, it is possible to operate in parameter regimes where the off-resonant terms have only a small effect. Although our study of off-resonant terms is extensive, our analysis of their impact is not exhaustive because of the sheer number of such terms. Their impact and the parameter regimes where they are negligible could potentially be explored directly on the quantum simulator. In addition, for typical operating conditions, we estimate that decoherence from off-resonant light scattering may limit the simulation time (Appendix B 4). However, we note that the relative strength of coherent interaction to decoherence can be increased, for instance, by the choice of ion species and transition, by enhancing coherent coupling via parametric amplification [23] or by working at a different operating point for the optical dipole force. Nevertheless, to demonstrate the potential of this approach, in the following we present results obtained from numerical simulations of Eqs. (12) and (11) and neglect the decoherence and off-resonant terms.

A. Initialization and readout

To observe dynamical phases generated by Hamiltonian (12), the spins must be initialized in a state possessing a chiral spin texture with a nonzero order parameter, such as those shown in Fig. 1(a). In the case of the trapped-ion crystal, it is convenient to work with a normalized order

parameter Ψ defined as

$$\Psi(t) = \frac{2}{N}\sum_{j=1}^{N} \tilde{r}_j e^{i\phi_j} \langle \hat{\mathfrak{s}}_j^-(t)\rangle. \tag{13}$$

For engineering interactions, the ODF beatnote frequency μ_r is tuned to couple the spins, the drumhead c.m. mode, and the planar rotation. For preparing chiral initial states, we instead tune μ_r to only couple the spins to the planar rotation without involving the drumhead c.m. mode. By additionally tuning the beam waist w_{ODF} of the ODF lasers, both BCS- and BEC-like initial spin textures can be prepared. The initialization Hamiltonian is of the form

$$\hat{H}_{\mathrm{init}} = \frac{\Omega_0}{2}\sum_j e^{-r_j^2/w_{\mathrm{ODF}}^2} \tilde{r}_j (\hat{\mathfrak{s}}_j^+ e^{-i\phi_j} + \hat{\mathfrak{s}}_j^- e^{i\phi_j}), \tag{14}$$

where Ω_0 is an effective drive strength. This Hamiltonian drives single-spin rotations where the axis of rotation for ion j depends on the azimuthal angle ϕ_j in the rotating frame. Starting with all spins initialized in $|\uparrow\rangle_Z$, setting $w_{\mathrm{ODF}} \gg R$, and using a pulse area $\Omega_0 T = \pi$ results in a BCS-like spin texture [e.g., Fig. 1(a)] that can be used to observe phases I and II. Here, we have exploited the fact that the magnitude of the Rabi frequency increases with the radius so that the central spin is unaffected while the outermost spins are rotated to $|\downarrow\rangle_Z$. A BEC-like spin texture [e.g., Fig. 1(a)] can be engineered by setting $w_{\mathrm{ODF}} < R$ and starting with all spins in $|\downarrow\rangle_Z$. In this way, ions at the center, where $\tilde{r}_j \sim 0$, are unaffected, whereas ions at the crystal boundary are also left unchanged since the beam intensity tapers to zero. On the other hand, ions in the intermediate region experience some degree of spin rotation and thereby give rise to a BEC-like texture. For observing phase III dynamics, a BCS-like initial state with a sharp domain wall between $|\downarrow\rangle_Z$ and $|\uparrow\rangle_Z$ spins and a small value of $|\Psi(0)|$ is suitable [e.g., top panel of Fig. 2(c)] [4]. Starting with all spins in $|\downarrow\rangle_Z$, a domain wall can be realized by using an optical pumping beam to selectively address ions in the central region and prepare them in $|\uparrow\rangle_Z$. Next, a global $\pi/2$ pulse rotates $Z \to \mathcal{Z}$ so that ions in the central region and those outside are respectively prepared in $|\uparrow\rangle_{\mathcal{Z}}$ and $|\downarrow\rangle_{\mathcal{Z}}$. A small initial $|\Psi(0)|$ can then be induced by a short-time application of Hamiltonian (14). A detailed description of state initialization is presented in Appendix G.

Measurement of the real and imaginary parts of the order parameter is also enabled by Hamiltonian (14). To demonstrate this, we first introduce site-dependent orthogonal axes,

$$\begin{aligned} \hat{\mathbf{e}}_{\mathcal{X}_j'} &= \sin\phi_j \hat{\mathbf{e}}_{\mathcal{X}} - \cos\phi_j \hat{\mathbf{e}}_{\mathcal{Y}}, \\ \hat{\mathbf{e}}_{\mathcal{Y}_j'} &= \cos\phi_j \hat{\mathbf{e}}_{\mathcal{X}} + \sin\phi_j \hat{\mathbf{e}}_{\mathcal{Y}}, \end{aligned} \tag{15}$$

such that $\hat{\mathbf{e}}_{\mathcal{X}_j'} \times \hat{\mathbf{e}}_{\mathcal{Y}_j'} = \hat{\mathbf{e}}_{\mathcal{Z}}$. In terms of these axes, we can write

$$\mathrm{Re}[\Psi] = \frac{2}{N}\sum_j \tilde{r}_j \langle \hat{\mathfrak{s}}_j^{\mathcal{Y}_j'}\rangle, \qquad \mathrm{Im}[\Psi] = \frac{2}{N}\sum_j \tilde{r}_j \langle \hat{\mathfrak{s}}_j^{\mathcal{X}_j'}\rangle, \tag{16}$$

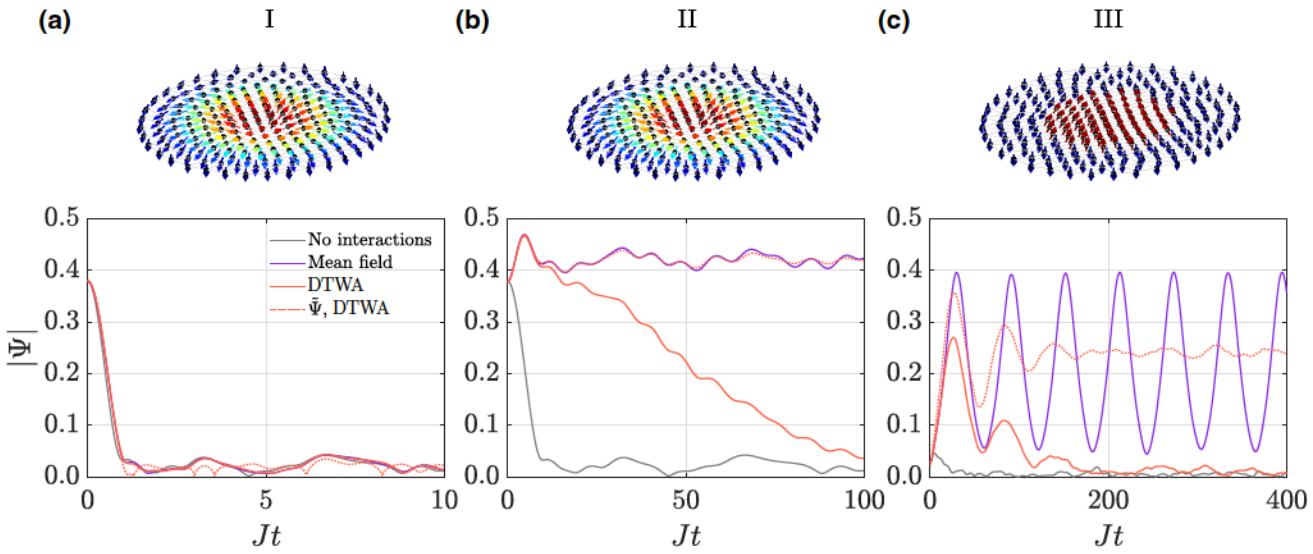

FIG. 2. Manifestation of dynamical phases in a 200 ion crystal. Initial BCS-like spin textures (top panels) and time evolution of $|\Psi(t)|$ in phases (a) I, (b) II, and (c) III. In (a) $K/J = 10$, while in (b) and (c) $K/J = 1$. The dynamics of $|\Psi(t)|$ are computed both using mean-field theory and the discrete truncated Wigner approximation (DTWA) method. The DTWA results show that the finite size of the crystal leads to a decay of $|\Psi(t)|$ even in phases II and III. However, the buildup of quantum correlations in these phases is captured by a second order parameter $\tilde{\Psi}$ [Eq. (20)]. In all cases, the decay of $|\Psi(t)|$ in the absence of interactions is plotted for reference. Crystal parameters are detailed in Appendix B and chiral spin states are initialized according to Appendix G.

and with $w_{\rm ODF} \gg R$, Hamiltonian (14) can be expressed as

$$\hat{H}_{\rm init} = \Omega_0 \sum_j \tilde{r}_j \hat{\mathfrak{s}}_j^{\mathcal{Y}'}. \tag{17}$$

After running the quantum simulation up to some time T, we evolve the system under Hamiltonian (17) for a further time t. This leads to

$$\begin{aligned}\langle \hat{\mathfrak{s}}_j^{\mathcal{Z}}(T+t)\rangle &= \langle \hat{\mathfrak{s}}_j^{\mathcal{Z}}(T)\rangle \cos(\Omega_0 \tilde{r}_j t) - \langle \hat{\mathfrak{s}}_j^{\mathcal{X}'}(T)\rangle \sin(\Omega_0 \tilde{r}_j t) \\ &\approx \langle \hat{\mathfrak{s}}_j^{\mathcal{Z}}(T)\rangle - (\Omega_0 \tilde{r}_j \langle \hat{\mathfrak{s}}_j^{\mathcal{X}'}(T)\rangle) t, \end{aligned} \tag{18}$$

where the approximation holds for short rotation times. Summing over all the ions, we get

$$\langle \hat{\mathfrak{J}}^{\mathcal{Z}}(T+t)\rangle - \langle \hat{\mathfrak{J}}^{\mathcal{Z}}(T)\rangle \approx -\frac{N\Omega_0}{2} \mathrm{Im}[\Psi(T)] t, \tag{19}$$

where $\hat{\mathfrak{J}}^{\mathcal{Z}} = \sum_j \hat{\mathfrak{s}}_j^{\mathcal{Z}}$. The imaginary part of the order parameter determines the rate of change of $\langle \hat{\mathfrak{J}}^{\mathcal{Z}}(T+t)\rangle$ as the rotation time t is increased. This quantity is accessible by a global fluorescence measurement after applying a global $\pi/2$ pulse to rotate $\mathcal{Z} \to Z$. Furthermore, a phase offset of $\pi/2$ can be introduced in Hamiltonian (14) by shifting the phase of the ODF beatnote, which can be used to measure $\mathrm{Re}[\Psi(T)]$ in a similar manner.

IV. PROBING THE DYNAMICAL PHASES

Having established protocols for initializing BCS-like and BEC-like initial states, for engineering interactions, and for measuring the order parameter, we now proceed to discuss how the dynamical phases can be observed in a crystal stored in a Penning trap. Figure 2 shows representative examples of the three dynamical phases, which are obtained using different BCS-like initial conditions and interaction strengths, the latter characterized by the ratio K/J. In each case, the initial spin texture is shown in the top panel. Phases I and II use the same initial spin texture but are obtained using $K/J = 10$ and $K/J = 1$, respectively. On the other hand, phase III is obtained using a different initial spin texture but with the same value of $K/J = 1$ as in phase II. The purple lines in Fig. 2 show the mean-field predictions for the time evolution of $|\Psi(t)|$ in each phase. The magnitude $|\Psi(t)|$ decays to 0 in phase I, saturates to a nonzero constant in phase II, and displays persistent oscillations in phase III. However, given the finite number of ions ($N = 200$), we are motivated to investigate the validity of mean-field theory in describing our system. Towards this end, we simulate the dynamics under $\hat{H}_{\rm 1ch}$ via the discrete truncated Wigner approximation (DTWA) method that accounts for the quantum noise of the initial state [24] (see Appendix E). The results of the DTWA simulations are shown by the red lines in Fig. 2. The DTWA and mean-field results agree well in phase I where the single-particle dephasing dominates the interactions. In contrast, the DTWA results deviate significantly from the mean-field predictions in phases II and III. In both cases, quantum noise causes the order parameter to eventually decay to zero in the long time limit.

Importantly, the decay of the mean-field order parameter $|\Psi(t)|$ in phases II and III is accompanied by the development of quantum correlations, which is captured in a more appropriate order parameter $\tilde{\Psi}$ defined as

$$\tilde{\Psi} = \frac{2}{N} \left| \sum_{j \neq k} \tilde{r}_j \tilde{r}_k \langle \hat{\mathfrak{s}}_j^+ \hat{\mathfrak{s}}_k^- \rangle e^{-i(\phi_j - \phi_k)} \right|^{1/2}. \tag{20}$$

We note that $\tilde{\Psi}$ is just a measure of the interaction part of Hamiltonian $\hat{H}_{\rm 1ch}$ [Eq. (12)]. While Ψ is the standard order parameter in superconductors, $\tilde{\Psi}$ could be thought of as the density of the Cooper pairs without concern to whether they are condensed. This is similar to the BEC phase of the BCS-BEC condensates, kept above the superconducting transition temperature and below the temperature of the formation of pairs [25]. Figure 2 shows that $\tilde{\Psi}$ stabilizes to a nonzero constant in phases II and III, indicating the persistence of dynamical p-wave superfluidity in these phases.

Even though the mean-field order parameter $|\Psi(t)|$ disappears at long times, the three phases can be distinguished in the short time dynamics of this observable. Figure 2 shows that, for $Jt \lesssim 20$, the mean-field and DTWA results are in approximate agreement in all three phases. The magnitude $|\Psi(t)|$ does not decay in phase II, whereas it exhibits strong amplification in phase III. In an experiment, the stabilization of superfluidity by interactions can be sharply demonstrated by comparing the dynamics of $|\Psi(t)|$ in the presence and absence of the ODF drive; in the absence of interactions, $|\Psi(t)|$ decays towards zero even on short time scales (gray lines in Fig. 2).

V. INFERRING TOPOLOGY

In contrast to s-wave superconductors, ground states and dynamical phases of p-wave superconductors can possess nontrivial topological properties. We now discuss how the topology of the dynamical phases can be probed in the ion simulator. For this study, we use the initial spin texture shown in Fig. 3(a), which is approximately BEC-like in the sense that the $\mathcal{Z}$ component of the spins first increases with radius, reaches a maximum, and then decreases with a further increase in radius. Figure 3(b) shows the winding number W [Eq. (10)] computed in mean-field theory as the ratio K/J is tuned for a crystal of $N = 200$ ions in the Penning trap (see Appendix F for details of this calculation on the discrete crystal lattice). The dynamical chemical potential μ_∞, which determines the rotating frame in which Eq. (10) is evaluated, is obtained from a

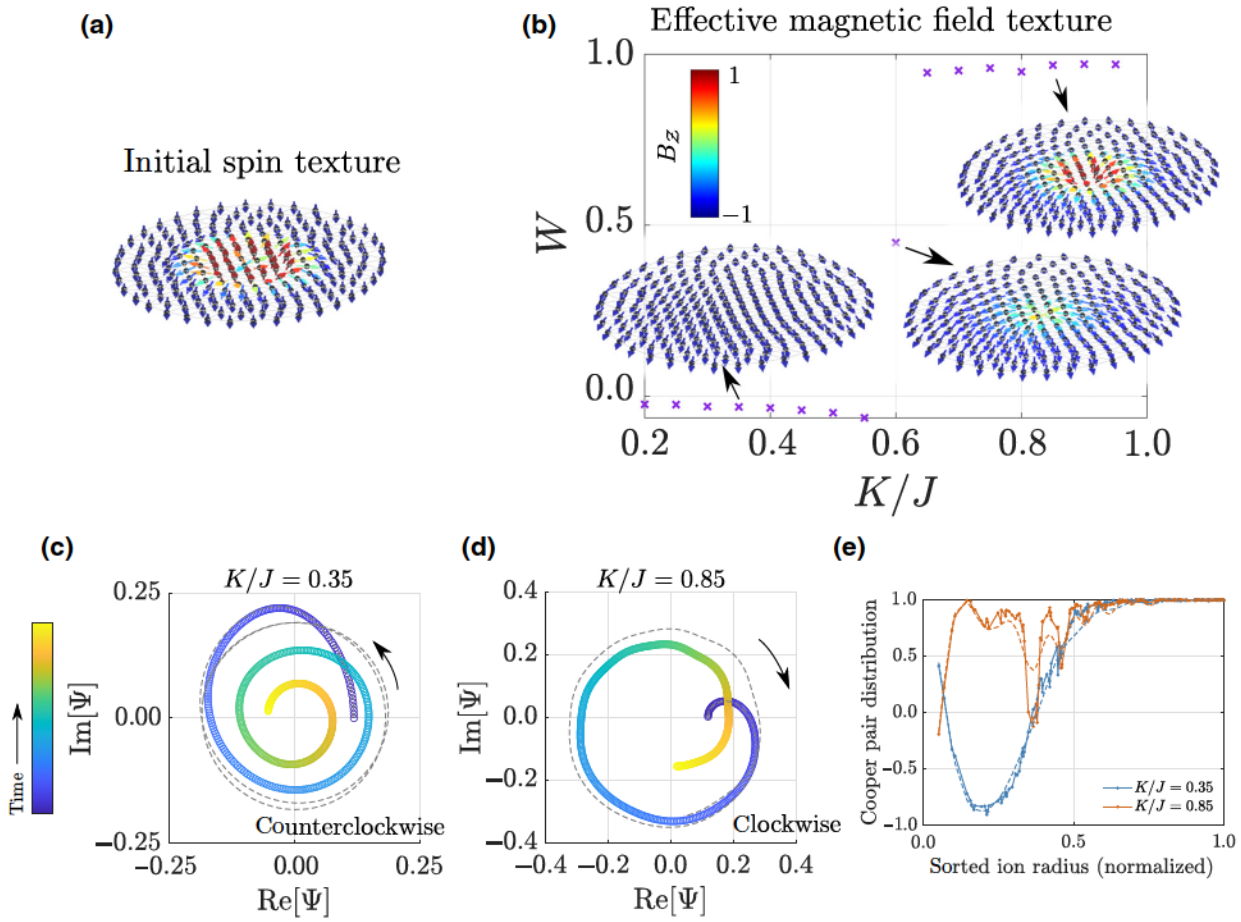

FIG. 3. Inferring topological properties of the dynamical phases. (a) Initial BEC-like spin texture. (b) Mean-field, long-time winding number of the effective magnetic field texture as the relative strength of the single-particle (K) and interaction (J) terms are varied. In the strong interaction case ($K/J < 0.6$), the texture is BEC-like and topologically trivial, while in the weak interaction case ($K/J > 0.6$), it is BCS-like and topologically nontrivial. Representative field textures are shown, where each arrow now indicates the unit vector of the effective magnetic field acting at that site, and the color code indicates the normalized B_Z component. (c),(d) The sense of rotation of the order parameter in the complex plane reveals the winding number of the underlying magnetic field texture. The topologically trivial (nontrivial) dynamical phase is associated with a counterclockwise (clockwise) rotation of $\Psi(t)$. While mean-field predicts a stable limit cycle (gray dashed line), DTWA calculations (colored circles) show the order parameter spiraling in towards the origin at long times (plotted here until $Jt = 100$). The color gradient indicates the arrow of time. (e) The Cooper pair distribution function (CPDF) displays an even (odd) number of zero crossings in the topologically trivial (nontrivial) case. These features are preserved even at times $Jt \sim 100$, when the order parameter has decayed considerably due to quantum fluctuations. For comparison, the dashed lines show the CPDF computed using mean-field theory. Crystal parameters are detailed in Appendix B and chiral spin states are initialized according to Appendix G.

Fourier transform of the time series of $\Psi(t)$. Representative examples of the effective magnetic field texture are also shown, which demonstrate the transition from a topologically trivial BEC-like texture ($K/J < 0.6$, $W \approx 0$) to a topologically nontrivial BCS-like texture ($K/J > 0.6$, $W \approx 1$). Remarkably, the topologically trivial and nontrivial phases can be distinguished by measurements of the real and imaginary parts of the order parameter. From Eq. (9), the sense of rotation of the order parameter in the complex plane—clockwise ($\mu_\infty > 0$) or counterclockwise ($\mu_\infty < 0$)—is a direct measurement of the sign of μ_∞ and, consequently, enables us to infer the BCS-like or BEC-like nature of the effective magnetic field texture. Figures 3(c) and 3(d) show that the sense of rotation of the order parameter is different for $K/J = 0.35$ and $K/J = 0.85$, clearly indicating the transition from a topologically trivial to a topologically nontrivial dynamical phase as the ratio K/J is tuned. While mean-field theory predicts the order parameter to precess with an approximately constant radius in the complex plane, the buildup of quantum correlations causes the order parameter to spiral in towards the origin at long times, consistent with Fig. 2(b). Nevertheless, the decay does not modify the topological nature of the dynamical phases.

The preservation of the topology in the regime where the order parameter is decaying can be confirmed by measuring the so-called Cooper pair distribution function (CPDF) $\gamma(\mathbf{p})$ [4]. This function characterizes the nonequilibrium distribution of the quasiparticle spectrum in the asymptotic steady state and provides information about the topology of the dynamical phases: the topology of the dynamical phase is trivial (nontrivial) if the number of zero crossings of this function is even (odd) [4]. In superconductors the CPDF can be measured via time-resolved, angle-resolved photoemission spectroscopy (ARPES) [26]. In the trapped-ion implementation, $\gamma(\mathbf{p})$ maps to $\gamma(\mathbf{r}_j, t)$, where $\mathbf{r}_j$ is the position of ion j, and corresponds to the projection of the local spin vector $\langle\hat{\mathfrak{s}}_j(t)\rangle$ onto the local effective magnetic field $\overline{\mathbf{B}}_j(t)$ at time t:

$$\gamma(\mathbf{r}_j, t) = \frac{\langle\bar{\hat{\mathfrak{s}}}_j(t)\rangle \cdot \overline{\mathbf{B}}_j(t)}{\sqrt{\langle\bar{\hat{\mathfrak{s}}}_j(t)\rangle \cdot \langle\bar{\hat{\mathfrak{s}}}_j(t)\rangle}\sqrt{\overline{\mathbf{B}}_j(t) \cdot \overline{\mathbf{B}}_j(t)}}. \tag{21}$$

Here, the overbar denotes that the spin and effective magnetic field are measured in a frame rotating at $2\mu_\infty$ and the denominator ensures that the quantity is the direction cosine of the spin vector with respect to the local magnetic field. Figure 3(e) shows the CPDF as a function of ion radius from the trap center for $K/J = 0.35$ and $K/J = 0.85$ computed by running the simulation up to a time $Jt = 100$. The CPDF is evaluated at the final time $Jt = 100$, while the value of μ_∞ is obtained from a Fourier transform of $\Psi(t)$ over the total simulation time. The solid curves in Fig. 3(e) have been computed accounting for quantum fluctuations, for which the decay of the order parameter is clearly visible in Figs. 3(c) and 3(d). We find that the parity of zero crossings of the CPDF enables an inference of the topology even after significant decay of the order parameter. We note that the CPDF can in principle be estimated from the experiment by site-resolved and time-resolved measurements of the spin components, from which both μ_∞ and the local $\overline{\mathbf{B}}_j(t)$ at each site can be estimated in phase II [see Eqs. (7) and the subsequent discussion in Sec. II].

VI. REALIZING A TWO-CHANNEL MODEL

So far, we have focused on a regime where the c.m. mode is coupled off resonantly to the spins and can hence be adiabatically eliminated, giving rise to an effective one-channel model description in terms of the Anderson spins alone. The c.m. mode plays the role of the bosonic molecular channel in the two-channel p-wave model. By suitably tuning the ODF difference frequency μ_r, a near-resonant coupling with the c.m. mode can be engineered, thereby enabling simulation of the more general two-channel Hamiltonian (11). Thus, our trapped-ion simulator allows the exploration of the distinct physical behaviors

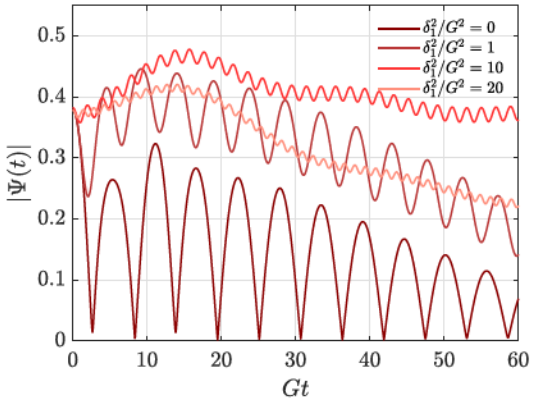

FIG. 4. Realizing the two-channel model. The drumhead c.m. mode plays the role of the molecular channel in the two-channel p-wave model. As the coupling to the c.m. mode is tuned from off resonant ($\delta_1^2/G^2 \gg 1$) to near resonance ($\delta_1^2/G^2 \sim 0$), its effects can be clearly observed in the time evolution of $|\Psi(t)|$. Here, we fix $B_1 = G/\sqrt{10}$ and vary δ_1 to obtain the different curves. Crystal parameters are detailed in Appendix B and chiral spin states are initialized according to Appendix G.

featured by both the one-channel and two-channel models in the same experimental setting. Figure 4 shows the time evolution of $|\Psi(t)|$ as the coupling to the c.m. mode is tuned from a far off-resonant regime ($\delta_1^2/G^2 \gg 1$) to the resonant regime ($\delta_1^2/G^2 \sim 0$). The curves are computed accounting for the initial quantum noise of the spins, which are initialized in a BCS-like state [top panel of Fig. 2(a)], as well as that of the c.m. mode, which is assumed to be initialized in the ground state. In the off-resonant regime, the behavior is similar to the one-channel model as the occupation of the c.m. mode remains small at all times. However, $|\Psi(t)|$ exhibits pronounced oscillatory behavior in the near-resonant and resonant regimes where excitations are strongly exchanged between the spins and the c.m. mode. Interestingly, these results indicate that, for fixed B_1, there is an optimal δ_1 in order to stabilize $|\Psi(t)|$ for a longer time. In addition to probing the role of the molecular channel, near-resonant coupling also enhances the interaction strength and hence may exhibit stronger signatures of the interaction dynamics in the time before sources of decoherence such as light scattering from the ODF beams kick in (Appendix B).

VII. CONCLUSION AND OUTLOOK

We have proposed a protocol to simulate the quench dynamics of $p + ip$ superfluids using ion crystals stored in a Penning trap. By utilizing the Anderson pseudospin mapping, we make a fermionic Hamiltonian amenable to simulation using spins encoded in the internal states of ions. In this way, we not only leverage the versatile toolbox of the trapped-ion platform but we also circumvent limitations that arise with direct simulations of the

fermionic model using ultracold quantum gases, where p-wave superfluids have been highly elusive to date.

We demonstrated how signatures of all three dynamical phases can be observed using crystals with about 200 ions. In the thermodynamic limit, the 2D $p + ip$ model becomes integrable and the dynamics is well described by mean-field theory. However, beyond-mean-field effects kick in at a finite number of fermions; the relatively small number of spins in the trapped-ion crystal naturally opens the avenue to observe beyond-mean-field effects in the quench dynamics of $p + ip$ superfluids and also facilitates the emulation of small superconducting grains [27].

We showed how the topological character of the dynamical phases can be inferred via the sense of rotation of the order parameter in the complex plane. Since our proposal maps the fermionic momentum on to the real-space position of ions, the addition of site-resolved detection of spins in the trap can provide time- and momentum-resolved measurements of the simulated system, analogous to techniques used in solid-state materials such as ARPES [28]. Along these lines, we showed how the Cooper pair distribution function can be used to probe the topology of the dynamical phase.

Although the $p + ip$ model is integrable, its quantum simulation is nevertheless an important milestone because this model represents an interacting system with nontrivial topological properties. Its experimental implementation in a controllable setting will provide access to observables that, although in principle are obtainable via the Bethe ansatz, can be challenging to compute in practice. While conventional mean-field theory is sufficient to describe the dynamics of the order parameter in the thermodynamic limit, a deep understanding of the underlying quantum behavior requires accessing observables that are beyond the reach of simple mean-field treatment. As an example, recent theory work has shown that if a $p + ip$ superconductor is quenched out of the critical point separating its topological and nontopological phases, its Loschmidt echo features singularities occurring periodically in time, a feature that is not expected to occur in s-wave superconductors [29]. It was found that the correct calculation of the Loschmidt echo requires more elaborate techniques that go beyond conventional mean-field theory. Trapped-ion simulators have already demonstrated the capability to measure Loschmidt echoes [14] and thus we expect that such simulators can probe not just finite-size quantum effects, but also beyond-mean-field effects that persist in the thermodynamic limit. As a second example, we show in Fig. 2 that, for a finite-size system, while the mean-field order parameter Ψ decays to zero, the many-body correlations are still captured in a more appropriate order parameter $\tilde{\Psi}$. This raises several interesting issues, such as the persistence and characterization of topology beyond mean-field winding numbers, the role of entanglement in stabilizing the dynamical phases, and the behavior of entanglement entropy (in momentum space) across the dynamical topological phase transition demonstrated in Fig. 3. These are issues that could be explored directly on the quantum simulator, since the computation of beyond-mean-field properties can be challenging in practice.

We also demonstrated that by tuning closer to resonance with the c.m. mode, a two-channel p-wave model can be realized and the nonzero occupation of a molecular channel can be additionally simulated and investigated. It will be interesting to explore conditions where a dynamically active molecular channel can enhance superfluidity [30], in a way reminiscent of analogous phenomena recently studied in solid-state quantum optics [31–41]. For example, our system can be used to study the response when the c.m. mode (i.e., the molecular channel) is driven or even squeezed via parametric amplification [23,42]. Furthermore, although we have considered a regime where the other drumhead modes are off resonant, strong spin-mode coupling can lead to weak excitations of more than a single mode, leading to the emergence of spatial inhomogeneities than can emulate the phenomenon of Cooper pair turbulence [43].

Beyond the simulation of $p + ip$ superconductors, trapped ions could also be used to study further exotic superconducting systems such as chiral $d_{x^2-y^2} + id_{xy}$ superfluids [44]. Such systems can be simulated in the Penning trap by engineering the phase of the ODF beams to have spatial variations, which is possible with the use of deformable mirrors [45].

Finally, we note that the fermionic statistics of the original p-wave model is not present in the corresponding spin mapping, and therefore our proposal cannot be used to produce Majorana fermions [46,47]. However, the protocols we have developed can be used to both produce skyrmionic spin textures as well as stabilize them using interactions, which could find applications in demonstrating skyrmion qubits for quantum computing [48].

ACKNOWLEDGMENTS

We thank Allison Carter for providing estimates for the decoherence rates from light scattering. We thank Diego Barberena and Bryce Bullock for a careful reading and comments on the manuscript. This work is supported by the European Union's Horizon 2020 research and innovation program under Grant Agreements No. 817482 (Pasquans), by the Simons Collaboration on Ultra-Quantum Matter, which is a grant from the Simons Foundation (651440, P. Z.), and by LASCEM via AFOSR No. 64896-PH-QC. Support is also acknowledged from the AFOSR under Grants No. FA9550-18-1-0319 and No. FA9550-19-1-0275, by the NSF PHY-1820885, NSF JILA-PFC PHY-1734006, QLCI-OMA-2016244, by the U.S. Department of Energy, Office of Science, National Quantum Information Science Research Centers, Quantum

Systems Accelerator, and by NIST. J.J.B. acknowledges support from the DARPA ONISQ program and AFOSR under Grant No. FA9550-201-0019.

APPENDIX A: DERIVATION OF EFFECTIVE HAMILTONIANS

We show how the combination of ODF and Raman beams with suitable geometries leads to effective one-channel and two-channel models for p-wave interactions in ion crystals stored in a Penning trap.

1. Optical dipole force with tilted wave vectors

The Hamiltonian corresponding to only the ODF interaction is

$$\hat{H} = \sum_{j=1}^{N} \omega_s \hat{s}_j^Z + \sum_{n=1}^{N} \omega_n \hat{a}_n^\dagger \hat{a}_n + 2\sum_{j=1}^{N} \delta_{\mathrm{AC}} \sin(\Delta k_x x_j + \Delta k_z \hat{z}_j - \mu_r t)\hat{s}_j^Z, \quad \text{(A1)}$$

where ω_s is the spin transition frequency, δ_{AC} is the strength of the optical dipole force, $\Delta\mathbf{k} = \Delta k_x \hat{\mathbf{e}}_x + \Delta k_z \hat{\mathbf{e}}_z$ is the difference wave vector of the ODF beams, and μ_r is their difference frequency. The out-of-plane motion is treated quantum mechanically and is represented by the operator $\hat{z}_j$. In terms of the drumhead modes, it can be expressed as

$$\Delta k_z \hat{z}_j = \sum_{n=1}^{N} \eta_n \mathcal{M}_{jn}(\hat{a}_n + \hat{a}_n^\dagger), \quad \text{(A2)}$$

where $\hat{a}_n, \hat{a}_n^\dagger$ are annihilation and creation operators for mode n with frequency ω_n, $\eta_n = \Delta k_z \sqrt{\hbar/(2m\omega_n)}$ is the Lamb-Dicke parameter, m is the ion mass, and $\mathcal{M}_{jn}$ is the displacement of ion j under the influence of mode n. In contrast, the in-plane motion is dominated by the crystal rotation and is represented by the classical coordinate $x_j(t) = r_j \cos(\omega_r t + \phi_j)$, where r_j is the distance of the ion from the trap center and ϕ_j is the azimuthal angle in the rotating frame.

Note on planar modes.—The complete planar motion consists of N cyclotron modes and N $\mathcal{E} \times \mathcal{B}$ modes whose motion is superposed on the crystal rotation. The cyclotron modes have high frequency and low amplitude, so we expect their impact to be negligible. The amplitude of the $\mathcal{E} \times \mathcal{B}$ modes can be appreciable, but they only couple weakly and off resonantly to the lasers with our choice of parameters, so their expected impact is still small.

2. Copropagating Raman beams

We now introduce a pair of Raman beams that drive resonant two-photon transitions between the spin states. The beams are assumed to be copropagating so that their difference wave vector approximately vanishes [49] and hence does not induce any spin-motion coupling. In a frame rotating at ω_s, the total Hamiltonian including the ODF and the Raman beams is

$$\hat{H} = \sum_{j=1}^{N} B_j \hat{s}_j^X + \sum_{n=1}^{N} \omega_n \hat{a}_n^\dagger \hat{a}_n + 2\sum_{j=1}^{N} \delta_{\mathrm{AC}} \sin(\Delta k_x x_j + \Delta k_z \hat{z}_j - \mu_r t)\hat{s}_j^Z. \quad \text{(A3)}$$

Here, B_j is the effective two-photon Rabi frequency at the site of ion j. Assuming a beam waist $w \gg R$ for the Raman lasers, where R is the crystal radius, we can approximate $B_j \approx B_0 - B_0 r_j^2/w^2$.

We now analyze the spin dynamics in a rotated spin space such that $\hat{\mathfrak{s}}_{\mathcal{Z}} \equiv -\hat{s}_X$ and $\hat{\mathfrak{s}}_{\mathcal{X}} \equiv \hat{s}_Z$. Further transforming to a frame rotating at B_0, the Hamiltonian in the rotated spin space is

$$\hat{H} = \sum_{j=1}^{N} B_0 \frac{r_j^2}{w^2} \hat{\mathfrak{s}}_j^{\mathcal{Z}} + \sum_{n=1}^{N} \omega_n \hat{a}_n^\dagger \hat{a}_n + \sum_{j=1}^{N} \delta_{\mathrm{AC}} \sin(\Delta k_x x_j + \Delta k_z \hat{z}_j - \mu_r t) \times (\hat{\mathfrak{s}}_j^+ e^{-iB_0 t} + \hat{\mathfrak{s}}_j^- e^{iB_0 t}). \quad \text{(A4)}$$

We can now see the twofold role played by the Raman drive: by providing a splitting $2B_0$ between $\hat{\mathfrak{s}}_j^+$ and $\hat{\mathfrak{s}}_j^-$, it will enable retention of only desired interactions and enable "rotating out" unwanted interactions. Second, the beam waist w acts as a knob to tune the single-particle dispersion.

3. Small-angle approximation

We now consider the sine function appearing in Eq. (A4). For three arguments $A = \Delta k_x x_j, B = \Delta k_z \hat{z}_j, C = -\mu_r t$, we can expand

$$\sin(A+B+C) = \sin(A+B)\cos(C) + \cos(A+B)\sin(C). \quad \text{(A5)}$$

We assume that $A, B \ll 1$ and expand the relevant trigonometric functions in the small-angle limit. The result, correct to second order in A, B, is

$$\sin(A+B+C) \approx (A+B)\cos C + \left(1 - \frac{A^2+B^2}{2} - AB\right)\sin C. \quad \text{(A6)}$$

4. Obtaining the two-channel model

We express the resonance requirements as a sum of frequencies appearing in the argument of complex exponentials multiplying each interaction term. To do so, we first note that the motion along x can be written as $x_j = r_j \cos(\omega_r t + \phi_j) = (r_j/2)(e^{i(\omega_r t+\phi_j)} + e^{-i(\omega_r t+\phi_j)})$, while the motion along z can be expanded as

$$\Delta k_z \hat{z}_j(t) = \sum_{n=1}^{N} \eta_n \mathcal{M}_{jn}(\hat{a}_n e^{-i\omega_n t} + \hat{a}_n^\dagger e^{i\omega_n t}). \tag{A7}$$

This expansion assumes that we have moved to an interaction picture with respect to the free phonon frequencies ω_n. The homogeneous Raman drive sets a frequency B_0 for the spins as seen from Eq. (A4). Finally, the terms $\cos(-\mu_r t), \sin(-\mu_r t)$ can be expanded with complex exponentials of the form $e^{\pm i\mu_r t}$. For discussing the resonance requirements (see Appendix C), we neglect the small contribution arising from the spatially inhomogeneous component of the Raman beams, i.e., we assume that the beam waist $w \to \infty$.

We tune μ_r to selectively induce a coupling between the spins (B_0), the drumhead c.m. mode (ω_1), and the planar rotation (ω_r). In particular, we adjust μ_r such that $B_0 - \mu_r + \omega_1 + \omega_r = \delta_1$. Then, the only near-resonant term stems from the $AB\sin C$-type term in Eq. (A6), and is of the form

$$\hat{H}_{\rm I} = -\sum_{j=1}^{N} \frac{G}{i\sqrt{N}} \tilde{r}_j (\hat{\mathfrak{s}}_j^- \hat{a}_1^\dagger e^{i(\delta_1 t+\phi_j)} - \hat{\mathfrak{s}}_j^+ \hat{a}_1 e^{-i(\delta_1 t+\phi_j)}), \tag{A8}$$

where $\tilde{r}_j = r_j/R$ is the ion radius normalized to the crystal radius R (assuming a nearly circular crystal) and G is given by

$$G = \frac{\delta_{\rm AC}\eta_1(\Delta k_x R)}{4}. \tag{A9}$$

Here, $\eta_1 = \Delta k_z\sqrt{\hbar/(2m\omega_1)}$ is the Lamb-Dicke parameter for the c.m. mode. The quantity $\Delta k_x R$ can be thought of as an effective Lamb-Dicke parameter for the in-plane motion. We will later consider the effect of off-resonant terms in Appendices C and D.

The above analysis is carried out assuming that the beam waist of the Raman lasers $w \to \infty$. Restoring a finite w and performing a frame transformation for the c.m. mode, we arrive at the effective Hamiltonian

$$\hat{H}_{\rm 2ch} = \sum_{j=1}^{N} B_1 \tilde{r}_j^2 \hat{\mathfrak{s}}_j^z + \delta_1 \hat{a}_1^\dagger \hat{a}_1 - \sum_{j=1}^{N} \frac{G}{i\sqrt{N}} \tilde{r}_j (\hat{\mathfrak{s}}_j^- \hat{a}_1^\dagger e^{i\phi_j} - \hat{\mathfrak{s}}_j^+ \hat{a}_1 e^{-i\phi_j}), \tag{A10}$$

where $B_1 = B_0 R^2/w^2$.

5. Effective spin-exchange interaction

We now eliminate the c.m. mode from Eq. (A10) using effective Hamiltonian theory [21]. We express energy resonance requirements once again as complex exponentials by defining $\delta_1^j = \delta_1 - B_1\tilde{r}_j^2$. Using a frame transformation for the spins and the c.m. mode, Eq. (A10) can be written as

$$\hat{H}_{\rm I} = -\sum_{j=1}^{N} \frac{G}{i\sqrt{N}} \tilde{r}_j (\hat{\mathfrak{s}}_j^- \hat{a}_1^\dagger e^{i(\delta_1^j t+\phi_j)} - \hat{\mathfrak{s}}_j^+ \hat{a}_1 e^{-i(\delta_1^j t+\phi_j)}). \tag{A11}$$

By assuming that the δ_1^j are large compared to the maximum interaction strength G, a spin-spin Hamiltonian can be derived using effective Hamiltonian theory. The result is

$$\hat{H}_{\rm eff} = \sum_{j,k=1}^{N} \frac{G^2}{Nh(\delta_1^j, \delta_1^k)} \tilde{r}_j \tilde{r}_k [\hat{a}_1^\dagger \hat{\mathfrak{s}}_j^- e^{i(\delta_1^j t+\phi_j)}, \hat{a}_1 \hat{\mathfrak{s}}_k^+ e^{-i(\delta_1^k t+\phi_k)}], \tag{A12}$$

where $h(a,b)$ is the harmonic mean of a, b. The commutator evaluates to

$$[\hat{a}_1^\dagger \hat{\mathfrak{s}}_j^-, \hat{\mathfrak{s}}_k^+ \hat{a}_1] = \begin{cases} -\hat{\mathfrak{s}}_j^- \hat{\mathfrak{s}}_k^+, & j \neq k, \\ -2\hat{a}_1^\dagger \hat{a}_1 \hat{\mathfrak{s}}_j^z - \hat{\mathfrak{s}}_j^+ \hat{\mathfrak{s}}_j^-, & j = k. \end{cases} \tag{A13}$$

The term containing $\hat{a}_1^\dagger \hat{a}_1$ can be neglected if the c.m. mode is initially in the ground state such that $\langle \hat{a}_1^\dagger \hat{a}_1 \rangle = 0$. Since the number operator of the c.m. mode only appears in the $j = k$ term, a small nonzero thermal occupation of the c.m. mode only changes the single-particle dispersion (kinetic energy) and does not affect the interaction terms. Therefore, it does not affect the ability to see the distinct dynamical phases in an experiment.

The effective Hamiltonian is therefore

$$\hat{H}_{\rm eff} = -\sum_{j,k=1}^{N} \frac{G^2}{Nh(\delta_1^j, \delta_1^k)} \tilde{r}_j \tilde{r}_k \hat{\mathfrak{s}}_j^+ \hat{\mathfrak{s}}_k^- e^{-i[(\delta_1^j - \delta_1^k)t + (\phi_j - \phi_k)]}. \tag{A14}$$

The time dependence can be removed via a frame transformation to give

$$\hat{H}_{\rm eff} = \sum_{j=1}^{N} \left(B_1 \tilde{r}_j^2 - \frac{G^2}{N\delta_1^j} \tilde{r}_j^2 \right) \hat{\mathfrak{s}}_j^z - \sum_{j=1}^{N} \sum_{k \neq j} \frac{G^2}{Nh(\delta_1^j, \delta_1^k)} \tilde{r}_j \tilde{r}_k \hat{\mathfrak{s}}_j^+ \hat{\mathfrak{s}}_k^- e^{-i(\phi_j - \phi_k)}. \tag{A15}$$

Since $\delta_1 \gg G^2/\delta_1$ and B_1 is comparable to the latter frequency, as a first approximation we can assume that $\delta_1^j \approx \delta_1^k \approx \delta_1$ and neglect site dependency in the denominators of the effective frequencies. This leads to the following Hamiltonian for the one-channel model:

$$\hat{H}_{1\mathrm{ch}} = K \sum_{j=1}^{N} \tilde{r}_j^2 \hat{\mathfrak{s}}_j^z - \frac{J}{N} \sum_{j=1}^{N} \sum_{k \neq j} \tilde{r}_j \tilde{r}_k \hat{\mathfrak{s}}_j^+ \hat{\mathfrak{s}}_k^- e^{-i(\phi_j - \phi_k)} \tag{A16}$$

with $J = G^2/\delta_1$ and $K = B_1 - J/N$. We note that the total magnetization $\hat{\mathfrak{J}}^z = \sum_j \hat{\mathfrak{s}}_j^z$ is conserved by this Hamiltonian.

APPENDIX B: EXPERIMENTAL PARAMETERS FOR IMPLEMENTATION

In this section, we provide experimental parameters for implementing our proposal. These parameters are based on settings used in the NIST Penning trap, where 2D crystals of tens to hundreds of $^9Be^+$ ions are routinely prepared for quantum simulation and sensing.

1. Trapping parameters

Two-dimensional crystals of $^9Be^+$ ions are formed in the Penning trap by a combination of an electric quadrupole field providing axial confinement and a strong axial magnetic field $\mathcal{B} \approx 4.46$ T [cyclotron frequency $\omega_c/(2\pi) \approx 7.6$ MHz] that aids in radial confinement. The spin-1/2 degree of freedom is encoded in two long-lived hyperfine levels of each $^9Be^+$ ion, i.e., $|\uparrow\rangle \equiv |2S_{1/2}, 1/2\rangle$ and $|\downarrow\rangle \equiv |2S_{1/2}, -1/2\rangle$. For a crystal with $N = 200$ ions, the crystal radius is $R \sim 100$ μm. Here we consider two sets of trapping parameters. In case A, we set the rotation frequency to $\omega_r/(2\pi) = 180$ kHz and choose the axial trapping frequency, which is also the drumhead c.m. frequency, to be $\omega_1/(2\pi) = 1.59$ MHz. In case B, we choose a faster rotating crystal with a higher axial trapping frequency, viz. $\omega_r/(2\pi) = 900$ kHz and $\omega_1/(2\pi) = 3.42$ MHz. In the following, we explicitly refer to the different cases when specifying parameters that are not the same in the two cases. While case A represents the commonly used trapping parameters, the reason we consider two sets of parameters will become clear in Appendix D, where we show that certain off-resonant terms are only negligible for the faster rotating crystal, i.e., case B. Nevertheless, we have used case-A trapping parameters for the figures presented in the main text, since those results have been obtained neglecting the off-resonant terms. In this situation, both case-A and case-B crystals give qualitatively similar results.

In general, both the ODF beams and the Raman beams intersect the crystal plane at a nonzero angle. However, for the quantum simulation, we require that these beams have a radially varying intensity profile in the crystal plane. This can be achieved by using laser beams with elliptical beam waists, whose cross section in the crystal plane will have a radial intensity profile.

2. ODF interaction

The optical dipole force is realized using a pair of lasers that intersect the crystal at approximately equal and opposite angles relative to the crystal plane; see Fig. 1(c). These lasers induce spatially varying ac Stark shifts on the pseudospin states by coupling these states to the $|2P_{3/2}\rangle$ manifold and give rise to a Hamiltonian of the form described in Eq. (A1).

From Fig. 1(c), the wave vectors of the ODF lasers are given by

$$\begin{aligned} \mathbf{k}_u &= (k\cos\theta)\hat{\mathbf{e}}_x - (k\sin\theta)\hat{\mathbf{e}}_z, \\ \mathbf{k}_l &= [k\cos(\theta+\delta\theta)]\hat{\mathbf{e}}_x + [k\sin(\theta+\delta\theta)]\hat{\mathbf{e}}_z, \end{aligned} \tag{B1}$$

where u, l denote the upper and lower ODF beams, respectively, and $k = |\mathbf{k}_u| = |\mathbf{k}_l|$. Denoting $k_x = k\cos\theta, k_z = k\sin\theta$, we can write

$$\begin{aligned} \mathbf{k}_u &= k_x\hat{\mathbf{e}}_x - k_z\hat{\mathbf{e}}_z, \\ \mathbf{k}_l &\approx (k_x - k_z\delta\theta)\hat{\mathbf{e}}_x + (k_z + k_x\delta\theta)\hat{\mathbf{e}}_z. \end{aligned} \tag{B2}$$

The difference wave vector can then be expressed as

$$\Delta\mathbf{k} = k_z\delta\theta\hat{\mathbf{e}}_x - (2k_z - k_x\delta\theta)\hat{\mathbf{e}}_z \equiv \Delta k_x\hat{\mathbf{e}}_x + \Delta k_z\hat{\mathbf{e}}_z. \tag{B3}$$

The wave-vector magnitude of each ODF laser is $k \approx 2\times 10^7 \mathrm{m}^{-1}$. The Lamb-Dicke parameter along the axial direction is $\eta_1 = \Delta k_z l_1^{zp}$, where $\Delta k_z \approx 2k\sin(\theta)$ is the difference wave vector along the z direction and $l_1^{zp} = \sqrt{\hbar/(2m\omega_1)}$ is the zero-point motion of the c.m. mode. Here, we have neglected the small correction to Δk_z that arises from a nonzero misalignment $\delta\theta$. To obtain a value η_1, the ODF lasers must be oriented at angles $\pm\theta$ with respect to the crystal plane, with $\theta = \sin^{-1}[\eta_1/(2kl_1^{zp})]$. For $\eta_1 \approx 0.3$, we find that $\theta \approx 23.4°$ for case A and $\theta \approx 35.7°$ for case B.

An analogous small parameter along the x direction is given by $\eta_x = \Delta k_x R$, where $\Delta k_x = k\delta\theta\sin\theta$ is the difference wave vector in the crystal plane. To obtain a value η_x, the required misalignment is given by $\delta\theta = \eta_x/(kR\sin\theta)$. For $\eta_x \approx 0.3$, we find that $\delta\theta \approx 0.017°$ for case A and $\delta\theta \approx 0.016°$ for case B. Experimentally, it is possible to control the tilt of the 1D optical lattice at the required level by monitoring sideband excitations at the rotation frequency. This technique has previously been used to align the optical dipole lattice wave vectors to be perpendicular to the crystal plane to better than 0.01° in the NIST Penning trap [50]. We note that wavefront control can be

facilitated in future work by using a spatial light modulator [45].

We assume that $\delta_{\mathrm{AC}}/(2\pi) \approx 40$ kHz. Then, the interaction strength G for the two-channel model is given by

$$\frac{G}{2\pi} = \frac{\delta_{\mathrm{AC}}\eta_1\eta_x}{4(2\pi)} = 900 \text{ Hz}. \tag{B4}$$

By assuming a detuning of $\delta_1/(2\pi) = 2$ kHz from the c.m. mode, we can arrive at the effective one-channel model coupling strength J as

$$\frac{J}{2\pi} = \frac{G^2}{\delta_1} = 405 \text{ Hz}. \tag{B5}$$

In this parameter regime, the ratio $\delta_1^2/G^2 \sim 5$ and, therefore, the simulation will have a small two-channel character to it in addition to the dominant one-channel model (see Fig. 4).

3. Raman beams

Two-photon Raman transitions between the pseudospin states can be engineered by introducing a pair of copropagating Raman lasers that couple these states to the $|2P_{3/2}\rangle$ manifold in a far detuned regime. The purpose of the Raman beams is twofold. First, the spatially homogeneous two-photon Rabi frequency B_0 breaks the symmetry between the $\hat{\mathbf{s}}^+$ and $\hat{\mathbf{s}}^-$ terms; see Eq. (A4). We take this value to be $B_0/(2\pi) = 10$ kHz. Second, the radially varying intensity of the Raman beams tunes the dispersion K of the spins. We estimate the scale of the required beam waist w as the value at which $K \approx J$, i.e.,

$$K \approx \frac{B_0 R^2}{w^2} = J \quad \Longrightarrow \quad w \approx 497\ \mu\text{m}. \tag{B6}$$

An alternative mechanism to generate a Raman beam intensity gradient is by utilizing the Doppler shifts arising from the crystal rotation. Although the Raman beams are copropagating, their difference wave vector $|\Delta k_R| \neq 0$ because of the frequency splitting ω_s of the spin states, i.e., $|\Delta k_R| = \omega_s/c$, where c is the speed of light in vacuum. Assuming that the Raman beams are propagating in the x-z plane and make an angle θ_R with the crystal plane, the Hamiltonian for a single ion interacting with the Raman beams is given by

$$\hat{H}_{R,j} = \omega_s \hat{s}_j^Z + \frac{B_0}{2}(\hat{s}_j^+ e^{i[|\Delta\mathbf{k}_R|\cos\theta_R x_j(t) - \Delta\omega_R t]} + \hat{s}_j^- e^{-i[|\Delta\mathbf{k}_R|\cos\theta_R x_j(t) - \Delta\omega_R t]}). \tag{B7}$$

In the Doppler-free case, two-photon resonance is satisfied by setting $\Delta\omega_R = \omega_s$. In this case, transforming to a frame rotating at ω_s leads to the interaction Hamiltonian

$$\hat{H}^I_{R,j} = \frac{B_0}{2}(\hat{s}_j^+ e^{i|\Delta\mathbf{k}_R|\cos\theta_R x_j(t)} + \hat{s}_j^- e^{-i|\Delta\mathbf{k}_R|\cos\theta_R x_j(t)}). \tag{B8}$$

The Doppler shift is time modulated because $x_j(t) = r_j\cos(\omega_r t + \phi_j)$. Defining $\eta_j^R = |\Delta\mathbf{k}_R|\cos\theta_R r_j$, we can use the Jacobi-Anger expansion to write

$$e^{-i\eta_j^R\cos(\omega_r t+\phi_j)} = \sum_{n=-\infty}^{\infty}(-i)^n J_n(\eta_j^R)e^{-in(\omega_r t+\phi_j)}, \tag{B9}$$

where $J_n(x)$ is the nth Bessel function of the first kind. The $n = 0$ term is then given by

$$\hat{H}^{I,(0)}_{R,j} = B_0 J_0(\eta_j^R)\hat{s}_j^X \approx B_0\left(1 - \frac{(\eta_j^R)^2}{4}\right)\hat{s}_j^X = \left(B_0 - \frac{B_0\omega_s^2 R^2}{4c^2}\tilde{r}_j^2\right)\hat{s}_j^X. \tag{B10}$$

The approximation is valid for $(\eta_j^R)^2 \ll 1$. To verify this, we consider the situation when the largest value of η_j^R occurs, i.e., when $\theta_R = 0$ and $r_j = R \sim 100$ μm. Using $\omega_s/(2\pi) = 124$ GHz, we estimate $\eta_j^R \approx 0.26$ and $(\eta_j^R)^2 \approx 0.067 \ll 1$. The achievable value of B_1 in this case is given by

$$B_1 = \frac{\omega_s^2 R^2}{4c^2}B_0 \approx 0.017 B_0 \approx 2\pi \times 170 \text{ Hz}, \tag{B11}$$

where we have used $B_0/(2\pi) = 10$ kHz. Therefore, it appears that B_1 can be partially realized even without a beam waist by simply exploiting the crystal rotation.

We note that the dispersion B_1 arising from the Doppler shifts can also be achieved if Raman beams are replaced with a microwave drive that is tilted with respect to the spatial z axis. Such an implementation may be simpler and will also eliminate off-resonant scattering from the Raman beams (see below). However, the long wavelength of microwaves precludes control of the beam waist at the 100-μm level for additional tuning of B_1 that may be required for some aspects of our proposal.

4. Decoherence from off-resonant light scattering

We separately estimate the contributions from the ODF beams and the Raman beams and find them to be [51,52]

$$\frac{\Gamma_{\mathrm{ODF}}}{2\pi} \approx 38 \text{ Hz}, \qquad \frac{\Gamma_{\mathrm{Raman}}}{2\pi} \approx 15 \text{ Hz}. \tag{B12}$$

The total decoherence rate is then $\Gamma_{\mathrm{tot}}/(2\pi) = (\Gamma_{\mathrm{ODF}} + \Gamma_{\mathrm{Raman}})/(2\pi) \approx 53$ Hz.

With the chosen parameters, we estimate the typical time up to which the simulation can be run as $Jt \approx$

$J(1/\Gamma_{\rm tot}) \sim 7.6$. As we mention in the main text, the ratio of the coherent interaction to the decoherence rate can be enhanced by a number of means, including choosing a different ion species and transition, enhancing coherent coupling by parametric amplification, and by working at a different ODF operating point.

We note that because of the multilevel structure of the electronic excited states, the full decoherence model for the ODF beams and for the Raman beams contains a number of independent decay channels with nontrivial rates and jump operators that are strongly modified by multilevel interference effects. Although we consider the full decoherence model [51,52], we have only roughly estimated the decoherence rate by inspecting analytical equations for the rate of decay of individual spin components. In the future, a detailed study of the impact of decoherence can be performed for specific experimental settings by including the full decoherence model in the numerical simulation.

APPENDIX C: ROTATING-WAVE APPROXIMATIONS

In deriving the two-channel model, we assumed that all other terms in the expansion equation (A6) could be considered rapidly oscillating. We now check whether this is true by first listing the various resonance conditions and estimating their values using real experimental parameters.

We first consider the term of the form $AB\sin C\hat{\mathfrak{s}}_j^-$, for which the possible arguments of the complex exponentials are (up to an overall sign, which gives the Hermitian conjugate process with $\hat{\mathfrak{s}}_j^+$)

$$\begin{aligned}
T_{11} &\equiv B_0 - \mu_r + \omega_n + \omega_r = \delta_n,\\
T_{12} &\equiv B_0 - \mu_r + \omega_n - \omega_r = \delta_n - 2\omega_r,\\
T_{13} &\equiv B_0 - \mu_r - \omega_n + \omega_r = \delta_n - 2\omega_n,\\
T_{14} &\equiv B_0 - \mu_r - \omega_n - \omega_r = \delta_n - 2\omega_n - 2\omega_r,\\
T_{15} &= B_0 + \mu_r + \omega_n + \omega_r = \delta_n + 2\mu_r,\\
T_{16} &\equiv B_0 + \mu_r + \omega_n - \omega_r = \delta_n + 2\mu_r - 2\omega_r,\\
T_{17} &\equiv B_0 + \mu_r - \omega_n + \omega_r = \delta_n + 2\mu_r - 2\omega_n,\\
T_{18} &\equiv B_0 + \mu_r - \omega_n - \omega_r = -\delta_n + 2B_0. \qquad \text{(C1)}
\end{aligned}$$

We next consider the term of the form $B^2\sin C\hat{\mathfrak{s}}_j^-$. Here, we have

$$\begin{aligned}
T_{21} &\equiv B_0 - \mu_r + \omega_n + \omega_k = \delta_1 + (\omega_n + \omega_k) - (\omega_1 + \omega_r),\\
T_{22} &\equiv B_0 - \mu_r + \omega_n - \omega_k = \delta_1 + (\omega_n - \omega_k) - (\omega_1 + \omega_r),\\
T_{23} &\equiv B_0 - \mu_r - \omega_n + \omega_k = \delta_1 + (\omega_k - \omega_n) - (\omega_1 + \omega_r),\\
T_{24} &\equiv B_0 - \mu_r - \omega_n - \omega_k = \delta_1 - (\omega_n + \omega_k) - (\omega_1 + \omega_r),\\
T_{25} &\equiv B_0 + \mu_r + \omega_n + \omega_k = \delta_1 + 2\mu_r + (\omega_n + \omega_k)\\
&\quad - (\omega_1 + \omega_r),\\
T_{26} &\equiv B_0 + \mu_r + \omega_n - \omega_k = \delta_1 + 2\mu_r + (\omega_n - \omega_k)\\
&\quad - (\omega_1 + \omega_r),\\
T_{27} &\equiv B_0 + \mu_r - \omega_n + \omega_k = \delta_1 + 2\mu_r + (\omega_k - \omega_n)\\
&\quad - (\omega_1 + \omega_r),\\
T_{28} &\equiv B_0 + \mu_r - \omega_n - \omega_k = \delta_1 + 2\mu_r - (\omega_n + \omega_k)\\
&\quad - (\omega_1 + \omega_r). \qquad \text{(C2)}
\end{aligned}$$

Next, we consider terms of the form $A^2\sin C\hat{\mathfrak{s}}_j^-$. For these terms, we get

$$\begin{aligned}
T_{31} &\equiv B_0 - \mu_r + \omega_r + \omega_r = \delta_n + \omega_r - \omega_n,\\
T_{32} &\equiv B_0 - \mu_r + \omega_r - \omega_r = \delta_n - \omega_r - \omega_n,\\
T_{33} &\equiv B_0 - \mu_r - \omega_r + \omega_r = \delta_n - \omega_r - \omega_n,\\
T_{34} &\equiv B_0 - \mu_r - \omega_r - \omega_r = \delta_n - 3\omega_r - \omega_n,\\
T_{35} &\equiv B_0 + \mu_r + \omega_r + \omega_r = \delta_n + 2\mu_r + \omega_r - \omega_n,\\
T_{36} &\equiv B_0 + \mu_r + \omega_r - \omega_r = \delta_n + 2\mu_r - \omega_r - \omega_n,\\
T_{37} &\equiv B_0 + \mu_r - \omega_r + \omega_r = \delta_n + 2\mu_r - \omega_r - \omega_n,\\
T_{38} &\equiv B_0 + \mu_r - \omega_r - \omega_r = \delta_n + 2\mu_r - 3\omega_r - \omega_n. \qquad \text{(C3)}
\end{aligned}$$

Now, we consider terms of the form $\sin C\hat{\mathfrak{s}}_j^-$. Here, the complex exponentials are simply $T_{41} \equiv B_0 + \mu_r$ and $T_{42} \equiv B_0 - \mu_r$, which respectively evaluate to $\delta_n + 2\mu_r - \omega_n - \omega_r$ and $\delta_n - \omega_n - \omega_r$.

We now turn to the term of the form $B\cos C\hat{\mathfrak{s}}_j^-$. Here, we have the detunings

$$\begin{aligned}
T_{51} &\equiv B_0 - \mu_r + \omega_n = \delta_n - \omega_r,\\
T_{52} &\equiv B_0 - \mu_r - \omega_n = \delta_n - 2\omega_n - \omega_r,\\
T_{53} &\equiv B_0 + \mu_r + \omega_n = \delta_n + 2\mu_r - \omega_r,\\
T_{54} &\equiv B_0 + \mu_r - \omega_n = \delta_n + 2\mu_r - 2\omega_n - \omega_r. \qquad \text{(C4)}
\end{aligned}$$

Finally, we consider the term of the form $A\cos C\hat{\mathfrak{s}}_j^-$. Here, we get

$$\begin{aligned}
T_{61} &\equiv B_0 - \mu_r + \omega_r = \delta_n - \omega_n,\\
T_{62} &\equiv B_0 - \mu_r - \omega_r = \delta_n - 2\omega_r - \omega_n,\\
T_{63} &\equiv B_0 + \mu_r + \omega_r = \delta_n + 2\mu_r - \omega_n,\\
T_{64} &\equiv B_0 + \mu_r - \omega_r = \delta_n + 2\mu_r - 2\omega_r - \omega_n. \qquad \text{(C5)}
\end{aligned}$$

In order to estimate these expressions, we compute the equilibrium crystal structure for cases A and B, and obtain the drumhead mode spectrum to obtain the frequencies ω_n. In Table I, we provide the maximum and minimum values

TABLE I. Minimum and maximum values of various resonance conditions for both trapping parameters, viz. case A and case B. The frequencies are reported in units of kilohertz.

Term	Case A	Case B
T_{11}	(−524, −19)	(−505, −21)
T_{12}	(−884, −358)	(−2305, −1798)
T_{13}	(−3178, −2652)	(−6849, −6343)
T_{14}	(−3538, −3012)	(−8649, −8143)
T_{15}	(3032, 3558)	(8163, 8669)
T_{16}	(2672, 3198)	(6363, 6869)
T_{17}	(378, 904)	(1818, 2325)
T_{18}	(18, 544)	(18, 525)
T_{21}	(360, 1412)	(1514, 2528)
T_{22}	(−2294, −1242)	(−4830, −3817)
T_{23}	(−2294, −1242)	(−4830, −3817)
T_{24}	(−4948, −3896)	(−11 175, −10 162)
T_{25}	(3916, 4968)	(10 182, 11 195)
T_{26}	(1262, 2314)	(3837, 4850)
T_{27}	(1262, 2314)	(3837, 4850)
T_{28}	(−1392, −340)	(−2508, −1494)
T_{31}	(−1408, −1408)	(−2524, −2524)
T_{32}	(−1768, −1768)	(−4324, −4324)
T_{33}	(−1768, −1768)	(−4324, −4324)
T_{34}	(−2128, −2128)	(−6124, −6124)
T_{35}	(2148, 2148)	(6144, 6144)
T_{36}	(1788, 1788)	(4344, 4344)
T_{37}	(1788, 1788)	(4344, 4344)
T_{38}	(1428, 1428)	(2544, 2544)
T_{41}	(1788, 1788)	(4344, 4344)
T_{42}	(−1768, −1768)	(−4324, −4324)
T_{51}	(−704, −178)	(−1405, −898)
T_{52}	(−3358, −2832)	(−7749, −7243)
T_{53}	(2852, 3378)	(7263, 7769)
T_{54}	(198, 724)	(918, 1425)
T_{61}	(−1588, −1588)	(−3424, −3424)
T_{62}	(−1948, −1948)	(−5224, −5224)
T_{63}	(1968, 1968)	(5244, 5244)
T_{64}	(1608, 1608)	(3444, 3444)

possible for each of these terms and for cases A and B. If the maximum and minimum values are large compared to $|\delta_1|$ and have the same sign then there are no accidental resonances and the terms can be safely neglected. We have excluded the c.m. term when evaluating the range of T_{11} as this is precisely the term of interest with $\delta_1/(2\pi) \leq 2$ kHz. Although at first glance all of these terms appear to be far off resonant, we explore the impact of low-order off-resonant terms in a quantitative manner in the next section.

APPENDIX D: ONE-CHANNEL MODEL AND OFF-RESONANT TERMS

For simulating the one-channel model, we assumed that $\delta_1/(2\pi) = 2$ kHz constitutes a large detuning based on which the c.m. mode can be adiabatically eliminated. The resulting interaction is fourth order in the small parameters A, B of the small-angle expansion, Eq. (A6). This raises the question whether some of the other terms in Eq. (A6), although off resonant, could potentially compete with the effective one-channel interactions because they are of lower order in the small parameters. In this section, we consider the effect of terms that are zeroth and first order in the small parameters on the effective dynamics of the one-channel model. We also estimate off-resonant effects that arise from the second-order term $AB \sin C$ since some terms in this group are not very far off resonant.

1. The sin *C* term

This term is of the form

$$\hat{H}_4 = \sum_j \frac{\delta_{\rm AC}}{2i}(\hat{\mathfrak{s}}_j^+ e^{-i(\mu_r+B_j)t} + \hat{\mathfrak{s}}_j^- e^{-i(\mu_r-B_j)t}) + \text{H.c.} \tag{D1}$$

Using effective Hamiltonian theory (EHT) and assuming that $B_j \ll \mu_r$ and $B_j \approx B_0$ leads to

$$\hat{H}_{4,\rm eff} = \sum_j \frac{\delta_{\rm AC}^2 B_0}{\mu_r^2}\hat{\mathfrak{s}}_j^Z. \tag{D2}$$

This term represents a small ac Stark shift that leads to collective spin precession at a frequency of about 5 Hz for case A and about 0.9 Hz for case B. Hence, its effect can be considered negligible.

2. The *A* cos *C* term

This term is of the form

$$\begin{aligned}\hat{H}_6 = \sum_j \frac{\delta_{\rm AC}\eta_x\tilde{r}_j}{4}\Big(&\hat{\mathfrak{s}}_j^+ e^{-i[(\mu_r+\omega_r+B_j)t+\phi_j]} \\ &+ \hat{\mathfrak{s}}_j^+ e^{-i[(\mu_r-\omega_r+B_j)t-\phi_j]} + \hat{\mathfrak{s}}_j^- e^{-i[(\mu_r+\omega_r-B_j)t+\phi_j]} \\ &+ \hat{\mathfrak{s}}_j^- e^{-i[(\mu_r-\omega_r-B_j)t-\phi_j]}\Big) + \text{H.c.}\end{aligned} \tag{D3}$$

Using EHT leads to

$$\begin{aligned}\hat{H}_{6,\rm eff} = -\sum_j \frac{\delta_{\rm AC}^2\eta_x^2\tilde{r}_j^2}{8}\Bigg[&\frac{1}{\mu_r+\omega_r+B_j} + \frac{1}{\mu_r-\omega_r+B_j} \\ &- \frac{1}{\mu_r+\omega_r-B_j} - \frac{1}{\mu_r-\omega_r-B_j}\Bigg]\hat{\mathfrak{s}}_j^Z.\end{aligned} \tag{D4}$$

Assuming that $B_j \sim B_0 \ll \omega_r, \mu_r$, we get

$$\hat{H}_{6,\rm eff} = \sum_j \frac{\delta_{\rm AC}^2 B_0\eta_x^2\tilde{r}_j^2}{4}\left[\frac{1}{(\mu_r+\omega_r)^2} + \frac{1}{(\mu_r-\omega_r)^2}\right]\hat{\mathfrak{s}}_j^Z. \tag{D5}$$

This term results in a radius-dependent ac Stark shift. We estimate its maximal value by setting $\tilde{r}_j = 1$, for which we find a precession frequency of about 0.5 Hz for case A and about 0.04 Hz for case B. These are very small compared to the dispersion generated by the Raman beam waist and hence we neglect these terms.

3. The *B* cos *C* term

This term is of the form

$$\hat{H}_5 = \sum_{j,n} \frac{\delta_{\rm AC}\eta_n \mathcal{M}_{jn}}{2} \Big(\hat{\mathfrak{s}}_j^+ \hat{a}_n e^{-i(\mu_r + B_0 + \omega_n)t} + \hat{\mathfrak{s}}_j^+ \hat{a}_n^\dagger e^{-i(\mu_r + B_0 - \omega_n)t} + \hat{\mathfrak{s}}_j^- \hat{a}_n e^{-i(\mu_r - B_0 + \omega_n)t} + \hat{\mathfrak{s}}_j^- \hat{a}_n^\dagger e^{-i(\mu_r - B_0 - \omega_n)t} \Big) + \text{H.c.} \tag{D6}$$

For applying EHT, we evaluate the commutators

$$[\hat{\mathfrak{s}}_j^+ \hat{a}_n, \hat{\mathfrak{s}}_k^- \hat{a}_m^\dagger] = 2\hat{a}_m^\dagger \hat{a}_n \hat{\mathfrak{s}}_j^Z \delta_{jk} + \delta_{nm} \hat{\mathfrak{s}}_j^+ \hat{\mathfrak{s}}_k^-,$$

$$[\hat{\mathfrak{s}}_j^+ \hat{a}_n^\dagger, \hat{\mathfrak{s}}_k^- \hat{a}_m] = 2\hat{a}_m \hat{a}_n^\dagger \hat{\mathfrak{s}}_j^Z \delta_{jk} - \delta_{nm} \hat{\mathfrak{s}}_j^+ \hat{\mathfrak{s}}_k^-,$$

$$[\hat{\mathfrak{s}}_j^- \hat{a}_n, \hat{\mathfrak{s}}_k^+ \hat{a}_m^\dagger] = -2\hat{a}_m^\dagger \hat{a}_n \hat{\mathfrak{s}}_j^Z \delta_{jk} + \delta_{nm} \hat{\mathfrak{s}}_j^- \hat{\mathfrak{s}}_k^+,$$

$$[\hat{\mathfrak{s}}_j^- \hat{a}_n^\dagger, \hat{\mathfrak{s}}_k^+ \hat{a}_m] = -2\hat{a}_m \hat{a}_n^\dagger \hat{\mathfrak{s}}_j^Z \delta_{jk} - \delta_{nm} \hat{\mathfrak{s}}_j^- \hat{\mathfrak{s}}_k^+. \tag{D7}$$

We only consider the effective role of each term in the Eq. (D6) independently. With the assumption of ground-state cooling, we make the replacements $\hat{a}_m^\dagger \hat{a}_n \to 0$ and $\hat{a}_m \hat{a}_n^\dagger \to \delta_{nm}$. We then have the effective Hamiltonian

$$\hat{H}_{5,\rm eff} = -\sum_j \sum_n \frac{\delta_{\rm AC}^2 \eta_n^2 \mathcal{M}_{jn}^2}{4} \left[\frac{1}{\mu_r + B_0 + \omega_n} + \frac{1}{\mu_r + B_0 - \omega_n} - \frac{1}{\mu_r - B_0 + \omega_n} - \frac{1}{\mu_r - B_0 - \omega_n} \right] \hat{\mathfrak{s}}_j^Z - \sum_{j \neq k} \sum_n \frac{\delta_{\rm AC}^2 \eta_n^2 \mathcal{M}_{jn} \mathcal{M}_{kn}}{4} \left[\frac{1}{\mu_r + B_0 + \omega_n} - \frac{1}{\mu_r + B_0 - \omega_n} + \frac{1}{\mu_r - B_0 + \omega_n} - \frac{1}{\mu_r - B_0 - \omega_n} \right] \hat{\mathfrak{s}}_j^+ \hat{\mathfrak{s}}_k^-. \tag{D8}$$

As a first approximation, we neglect terms with $\mu_r + \omega_n$ in the denominator since they are small compared with terms that have $\mu_r - \omega_n$ in the denominator. Using the fact that $B_0 \ll \mu_r - \omega_n$, we arrive at the approximate effective Hamiltonian

$$\hat{H}_{5,\rm eff} = \sum_{j,k} J_{5,jk} \hat{\mathfrak{s}}_j^+ \hat{\mathfrak{s}}_k^-, \tag{D9}$$

where the interaction matrix J_5 has elements given by

$$J_{5,jk} = \begin{cases} \sum_n \dfrac{\delta_{\rm AC}^2 B_0 \eta_n^2 \mathcal{M}_{jn}^2}{2(\mu_r - \omega_n)^2}, & j = k, \\ \sum_n \dfrac{\delta_{\rm AC}^2 \eta_n^2 \mathcal{M}_{jn} \mathcal{M}_{kn}}{2(\mu_r - \omega_n)}, & j \neq k. \end{cases} \tag{D10}$$

The effective Hamiltonian $\hat{H}_{5,\rm eff}$ mediates achiral spin-exchange-type interactions that directly compete with the chiral spin-exchange that we wish to engineer. We study the impact of this term numerically in Fig. 5 for case A and case B using mean-field theory. We find that in case A this interaction causes $|\Psi(t)|$ to rapidly decay toward zero on short timescales, whereas in case B the impact of this term is rather small. From the form of the elements in the coupling matrix J_5, a larger rotation frequency ω_r increases the denominator, i.e., makes these terms smaller and hence their impact is smaller in case B.

4. The *AB* sin *C* term

The interaction giving rise to the two-channel model is present in this second-order term and was discussed previously. Here, we estimate the contribution of other interactions present in this term since some of them are not very far off resonant.

This term is of the form

$$\hat{H}_1 = -\sum_{j,n} \frac{\delta_{\rm AC} \eta_x \tilde{r}_j \eta_n \mathcal{M}_{jn}}{4i} \Big(\hat{\mathfrak{s}}_j^+ \hat{a}_n^\dagger e^{-i[(\mu_r - \omega_n - \omega_r + B_0)t - \phi_j]} + \hat{\mathfrak{s}}_j^+ \hat{a}_n^\dagger e^{-i[(\mu_r - \omega_n + \omega_r + B_0)t + \phi_j]} + \hat{\mathfrak{s}}_j^- \hat{a}_n^\dagger e^{-i[(\mu_r - \omega_n - \omega_r - B_0)t - \phi_j]} + \hat{\mathfrak{s}}_j^- \hat{a}_n^\dagger e^{-i[(\mu_r - \omega_n + \omega_r - B_0)t + \phi_j]} \Big) + \text{H.c.} \tag{D11}$$

In writing the above equation, we have already ignored the terms that have exponentials containing the combination $\mu_r + \omega_n$. Following a calculation similar to the *B* cos *C* term, we find an effective Hamiltonian given by

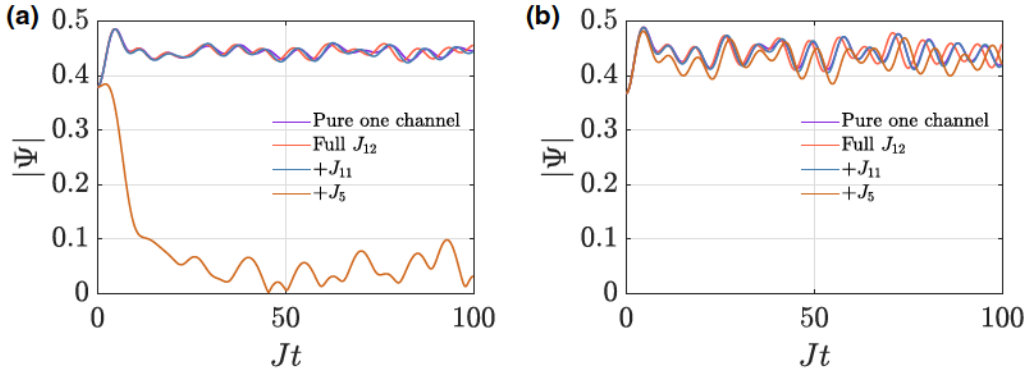

FIG. 5. Impact of off-resonant interactions on the one-channel model dynamics for crystals formed under two different trapping parameters: (a) case A and (b) case B (see Appendix B 1). In both cases, we progressively add terms to the pure one-channel model and study their impact. We add the following terms in the specified order: Chiral spin exchange by all modes (J_{12}), antichiral spin exchange by all modes (J_{11}), and achiral spin exchange by all modes (J_5). Here, we start from a BCS-like initial state [top panel of Fig. 2(a)] and use the experimental parameters discussed in Appendix B. We have used $B_1 \approx J$, where the value of $J/(2\pi) \approx 405$ Hz.

$$\hat{H}_{1,\text{eff}} = \sum_{j,k} J_{11,jk} \hat{\mathfrak{s}}_j^+ \hat{\mathfrak{s}}_k^- + \sum_{j,k} J_{12,jk} \hat{\mathfrak{s}}_j^+ \hat{\mathfrak{s}}_k^-, \tag{D12}$$

where the interaction matrices J_{11}, J_{12} have elements given by

$$J_{11,jk} = \begin{cases} \sum_n \dfrac{\delta_{\text{AC}}^2 \eta_x^2 \tilde{r}_j^2 \eta_n^2 \mathcal{M}_{jn}^2}{16(\delta_n - 2B_0)}, & j = k, \\ -\sum_n \dfrac{\delta_{\text{AC}}^2 \eta_x^2 \tilde{r}_j \tilde{r}_k \eta_n^2 \mathcal{M}_{jn} \mathcal{M}_{kn}}{16} \left[\dfrac{1}{\delta_n - 2B_0} + \dfrac{1}{\delta_n - 2\omega_r} \right] e^{i(\phi_j - \phi_k)}, & j \neq k, \end{cases}$$

$$J_{12,jk} = \begin{cases} -\sum_n \dfrac{\delta_{\text{AC}}^2 \eta_x^2 \tilde{r}_j^2 \eta_n^2 \mathcal{M}_{jn}^2}{16\delta_n}, & j = k, \\ -\sum_n \dfrac{\delta_{\text{AC}}^2 \eta_x^2 \tilde{r}_j \tilde{r}_k \eta_n^2 \mathcal{M}_{jn} \mathcal{M}_{kn}}{16} \left[\dfrac{1}{\delta_n - 2\omega_r} + \dfrac{1}{\delta_n} \right] e^{-i(\phi_j - \phi_k)}, & j \neq k. \end{cases} \tag{D13}$$

The J_{12} matrix now represents the chiral spin-exchange interactions arising from all drumhead modes. On the other hand, the J_{11} matrix describes antichiral interactions mediated by these modes. We estimate the impact of these terms numerically in Fig. 5 and find that they do not significantly impact the one-channel model dynamics in both cases A and B.

Our study of off-resonant interactions shows that trapping parameters can be found where the impact of these terms can be neglected for realizing the one-channel model. In the case of the two-channel model, preliminary numerical results indicate that, even in case A, the adverse impact of off-resonant terms on short timescales ($Gt \lesssim 30$) is reduced as the c.m. mode is brought near resonance, suggesting that two-channel dynamics could be probed even with case-A trapping parameters. The pure one-channel and pure two-channel model results presented in the main text have been computed using the case-A equilibrium crystal. We have checked that all the results for the case-B equilibrium crystal are qualitatively similar to the case-A results when off-resonant terms are neglected.

We end this section by noting that we have not extensively considered the impact of cross talk between different terms as well as the role of terms at third and higher orders in the small parameters, because of the sheer number of terms and their combinations. Their impact and the parameter regimes where they are negligible could potentially be explored directly on the quantum simulator.

APPENDIX E: NUMERICAL METHODS

While the classification of dynamical phases is based on a mean-field study in the thermodynamic limit, the

finite size of our system has motivated us to consider beyond-mean-field techniques for numerical solution. Here, we present the mean-field equations for the one-channel and two-channel models, discuss how we include the quantum noise of the initial state using the DTWA method, and benchmark the performance of DTWA using special crystals where the geometry allows for exact numerical solution of the Schrödinger equation.

1. Mean-field equations of motion for one-channel and two-channel models

In the mean-field theory for the one-channel model, we replace the spin vector operator $\hat{\mathfrak{s}}_j$ at each site j by a vector of c numbers $\mathfrak{s}_j \equiv (\mathfrak{s}_j^x, \mathfrak{s}_j^y, \mathfrak{s}_j^z)$. The commutation relations are replaced by Poisson brackets, $\{\mathfrak{s}_j^a, \mathfrak{s}_k^b\} = i\epsilon_{abc}\mathfrak{s}_j^c\delta_{jk}$. Defining $\mathfrak{s}_j^\pm = \mathfrak{s}_j^x \pm i\mathfrak{s}_j^y$, the dynamics under Hamiltonian (A16) are given by

$$\begin{aligned}\frac{d}{dt}\mathfrak{s}_j^+ &= iK\tilde{r}_j^2\mathfrak{s}_j^+ + iJ\tilde{r}_j\mathfrak{s}_j^z e^{i\phi_j}\Psi_j^*,\\ \frac{d}{dt}\mathfrak{s}_j^z &= -J\tilde{r}_j\,\mathrm{Im}[\mathfrak{s}_j^+ e^{-i\phi_j}\Psi_j],\end{aligned} \tag{E1}$$

where $\Psi_j = (2/N)\sum_{k\neq j}\tilde{r}_k\mathfrak{s}_k^- e^{i\phi_k}$.

To obtain the mean-field equations for the two-channel model governed by Hamiltonian (A10), we additionally replace the annihilation operator $\hat{a}_1$ of the c.m. mode by a complex amplitude α_1. The resulting equations are

$$\begin{aligned}\frac{d}{dt}\mathfrak{s}_j^+ &= iB_1\tilde{r}_j^2\mathfrak{s}_j^+ + \frac{2G}{\sqrt{N}}\alpha_1^*\mathfrak{s}_j^z\tilde{r}_j e^{i\phi_j},\\ \frac{d}{dt}\mathfrak{s}_j^z &= -\frac{2G}{\sqrt{N}}\tilde{r}_j\,\mathrm{Re}[s_j^+\alpha_1 e^{-i\phi_j}],\\ \frac{d}{dt}\alpha_1 &= -i\delta_1\alpha_1 + \frac{\sqrt{N}G}{2}\Psi,\end{aligned} \tag{E2}$$

with $\Psi = (2/N)\sum_j \tilde{r}_j\mathfrak{s}_j^- e^{i\phi_j}$.

For mean-field simulations, the above equations are numerically evolved starting from initial conditions where the c numbers are assigned the expectation values of the corresponding quantum operators in the initial state.

2. Accounting for initial quantum noise

For finite-size systems, quantum corrections to the mean-field dynamics become important. To explore their effects, we simulate the effects of the quantum noise of the initial state by evolving several trajectories under the mean-field equations starting from randomly drawn initial conditions. For the spin degrees of freedom, we first find the mean spin direction $\hat{\mathbf{e}}_j^\parallel$ in the initial state. Next, we identify two mutually orthogonal spin directions, $\hat{\mathbf{e}}_j^{\perp,1}, \hat{\mathbf{e}}_j^{\perp,2}$, in the plane perpendicular to the mean spin. The initial spin vector can then be written as

$$\mathfrak{s}_j = \mathfrak{s}_j^\parallel\hat{\mathbf{e}}_j^\parallel + \mathfrak{s}_j^{\perp,1}\hat{\mathbf{e}}_j^{\perp,1} + \mathfrak{s}_j^{\perp,2}\hat{\mathbf{e}}_j^{\perp,2}. \tag{E3}$$

For mean-field simulations, we set $\mathfrak{s}_j^\parallel = 1/2, \mathfrak{s}_j^{\perp,1} = \mathfrak{s}_j^{\perp,2} = 0$. To go beyond mean field, we use the prescription of the discrete truncated Wigner approximation [24], according to which $\mathfrak{s}_j^{\perp,1}$ and $\mathfrak{s}_j^{\perp,2}$ are independently and randomly chosen to be $\pm 1/2$ with equal probability.

In the case of the two-channel model, we additionally draw the complex amplitude α_1 from the Wigner distribution of the initial state of the c.m. mode, which we always assume is the motional ground state in this work. Therefore, the real and imaginary parts of α_1 are independently drawn from a Gaussian distribution with zero mean and a variance of 1/4.

3. Benchmarking the DTWA results

In the case of a real crystal in a Penning trap, the triangular lattice is only approximate and hence every ion is typically at a slightly different radius from the trap center. This makes an exact solution of the Schrödinger equation subject to Hamiltonian (A16) exponentially hard. Therefore, in order to test the reliability of the DTWA results, we test this technique on a hypothetical ideal crystal made of M concentric rings of ions, for which an exact numerical solution to the Schrödinger equation is feasible. We assume that the number of ions N_m in ring $m = 1, \ldots, M$ is given by $N_m = 6(m-1) + \delta_{m,1}$, which roughly mimics the lattice structure of closed-shell Penning trap crystals. Here, the first ring $m = 1$ is taken to be the single ion at the crystal center. For simplicity, we assume that the radius of the rings r_m grows linearly with ring index m with $r_1 = 0$.

For this model, we can define total angular momentum operators for each ring, $\hat{\mathfrak{J}}_m^\pm, \hat{\mathfrak{J}}_m^z$, as

$$\hat{\mathfrak{J}}_m^\pm = \sum_{j\in\text{ring }m}\hat{\mathfrak{s}}_j^\pm e^{\mp i\phi_j}, \qquad \hat{\mathfrak{J}}_m^z = \sum_{j\in\text{ring }m}\hat{\mathfrak{s}}_j^z. \tag{E4}$$

These operators are readily seen to obey the usual angular momentum commutation relations. In terms of these operators, the one-channel model (A16) can be expressed as

$$\hat{H}_{\text{eff}} = B_1\sum_{m=1}^{M}\tilde{r}_m^2\hat{\mathfrak{J}}_m^z - \frac{J}{N}\sum_{m,m'=1}^{M}\tilde{r}_m\tilde{r}_{m'}\hat{\mathfrak{J}}_m^+\hat{\mathfrak{J}}_{m'}^-. \tag{E5}$$

For a crystal with M rings, the total number of ions is $N(M) = 1 + 3M(M-1)$. The computational complexity is significantly reduced in the total angular momentum picture, because, for the initial states we consider, we only need to track the fully symmetric subspace of each ring. Therefore, the number of basis states in each ring is

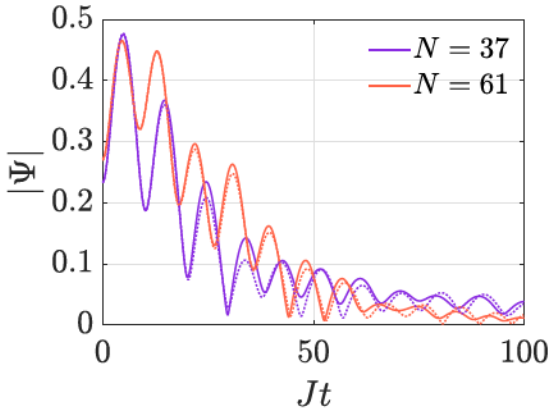

FIG. 6. Benchmarking the DTWA method. Solid lines are computed by numerical propagation of the Schrödinger equation, while the dotted lines are obtained using the DTWA method. Here, we assume that the crystal is made of perfectly concentric rings of ions and that the spin state is initialized in a BCS-like state [top panel of Fig. 2(a)]. Here, we have used the ratio $K/J = 1$.

reduced from 2^{N_m} to $N_m + 1$, thereby enabling the rapid simulation of exact dynamics for crystals with up to $M = 5$ rings [$N(5) = 61$ ions]. Figure 6 shows the excellent agreement of the DTWA calculation with the exact solution for crystals with $M = 4$ and $M = 5$ rings, confirming the validity of the DTWA technique for beyond-mean-field calculations in this work.

APPENDIX F: COMPUTATION OF WINDING NUMBERS

In continuous 2D space, the winding number of a unit vector field $\hat{\mathbf{u}}(x, y)$ is defined as the surface integral

$$W = \frac{1}{4\pi} \int dx\, dy\, \hat{\mathbf{u}} \cdot \left(\frac{d\hat{\mathbf{u}}}{dx} \times \frac{d\hat{\mathbf{u}}}{dy} \right). \tag{F1}$$

In the crystal, the winding number calculation must be carried out on a lattice with discrete sites. Here, the prescription is to identify triplets of neighbors by introducing a triangulation of the crystal lattice as shown in Fig. 7 [53]. We use the Delaunay triangulation, wherein triangles are formed between neighboring triplets in such a way that no vertex of the crystal lies inside the circumcircle of each triangle. For each triangle, we label the vertices A, B, C such that the directed edges give rise to a face normal pointing upward from the crystal plane, i.e., $\overrightarrow{AB} \times \overrightarrow{BC} \parallel \hat{\mathbf{e}}_z$. Having identified such ordered triplets of vertices, a solid angle Ω_{ABC} is introduced for each triangle, defined as

$$\tan\left(\frac{\Omega_{ABC}}{2}\right) = \frac{\hat{\mathbf{u}}_A \cdot (\hat{\mathbf{u}}_B \times \hat{\mathbf{u}}_C)}{1 + \hat{\mathbf{u}}_A \cdot \hat{\mathbf{u}}_B + \hat{\mathbf{u}}_B \cdot \hat{\mathbf{u}}_C + \hat{\mathbf{u}}_C \cdot \hat{\mathbf{u}}_A}. \tag{F2}$$

The winding number on the discrete lattice is obtained by summing the solid angle Ω_{ABC} over all triangles Δ_{ABC} of

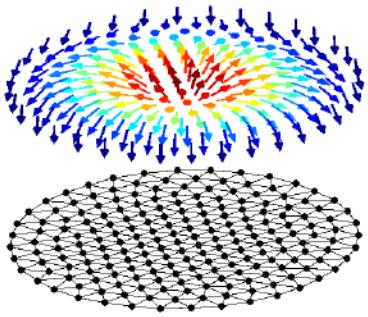

FIG. 7. Demonstration of Delaunay triangulation for a crystal with 200 ions. The triangulation is used to identify triplets of neighbors on the discrete lattice for computing the winding number of the spin texture (Q) or that of the effective magnetic field texture (W).

the triangulation:

$$W = \frac{1}{4\pi} \sum_{\Delta_{ABC}} \Omega_{ABC}. \tag{F3}$$

In the present work, we call the winding number Q if the vector field is taken as the spin texture, while we label it as W if the vector field is the effective magnetic field texture in the frame rotating at $2\mu_\infty$.

APPENDIX G: STATE INITIALIZATION

To generate chiral BCS-like and BEC-like initial states, we take advantage of the term of the form $A \cos C\hat{\mathfrak{s}}_j^-$ that is available in the small-angle expansion of the ODF interaction [Eq. (A6)]. This term describes a coupling of the spins with the planar rotation without involving the drumhead c.m. mode. We assume that the ODF lasers have a tunable beam waist w_{ODF}. By tuning $\mu_r = B_0 + \omega_r$ and ignoring rapidly oscillating terms, the effective interaction is given by

$$\hat{H}_{\mathrm{init}} = \sum_j \frac{\Omega_j}{2} (\hat{\mathfrak{s}}_j^+ e^{-i\phi_j} + \hat{\mathfrak{s}}_j^- e^{i\phi_j}), \tag{G1}$$

where $\Omega_j = \Omega_0 \tilde{r}_j e^{-r_j^2/w_{\mathrm{ODF}}^2}$ with $\Omega_0 = \delta_{\mathrm{AC}}(\Delta k_x R)/2$ and $\tilde{r}_j = r_j/R$. Hamiltonian $\hat{H}_{\mathrm{init}}$ describes noninteracting spins each undergoing rotation under a local magnetic field. Using the local axes introduced in Eqs. (15), we can compactly write

$$\hat{H}_{\mathrm{init}} = \sum_j \Omega_j \hat{\mathfrak{s}}_j^{y_j'}. \tag{G2}$$

For the initialization, we assume that the beam waist of the Raman beams is much larger than the crystal radius,

i.e., $w \gg R$, so that the dispersion arising from the spatial variation of the Raman beams can be neglected.

We now describe the initialization protocols for various cases that we discuss in the main text.

1. BCS initialization for phases I and II

We assume that the beam waists of the ODF lasers are much larger than the crystal radius, i.e., $w_{\mathrm{ODF}} \gg R$. Then, $\hat{H}_{\mathrm{init}}$ reduces to

$$\hat{H}_{\mathrm{init}} = \Omega_0 \sum_j \tilde{r}_j \hat{\mathfrak{s}}_j^{y'}. \tag{G3}$$

We initialize all spins in $|\uparrow\rangle_Z$ (i.e., in the rotated spin space) by an appropriate global $\pi/2$ pulse. Setting the maximum pulse area $\Omega_0 T = \pi$, the outermost spins are then rotated all the way to $|\downarrow\rangle_Z$ whereas the central spin is unaffected by virtue of the dependence of the Rabi frequency on $\tilde{r}_j$. Data shown in Figs. 2(a), 2(b), and 4 are obtained using this initial state.

2. BEC initialization for winding number studies

We assume that $w_{\mathrm{ODF}} < \sqrt{2}R$. The radial modulation of the Rabi frequency results in a maximum Rabi frequency Ω_{max} at radius r_{max}, which are respectively given by

$$\Omega_{\mathrm{max}} = \Omega_0 \frac{w_{\mathrm{ODF}}}{R\sqrt{2e}}, \qquad r_{\mathrm{max}} = \frac{w_{\mathrm{ODF}}}{\sqrt{2}}. \tag{G4}$$

Therefore, for $w_{\mathrm{ODF}} < \sqrt{2}R$, the maximum pulse area for a fixed rotation time T is experienced by a spin somewhere in the middle of the crystal. We initialize all spins in $|\downarrow\rangle_Z$. For the winding number study, we set the maximum pulse area $\Omega_{\mathrm{max}} T = \pi$ and use a beam waist $w_{\mathrm{ODF}} = 0.3R$, which ensures that a large number of the outer spins are negligibly rotated. This ensures that the winding number W is reasonably quantized. Data shown in Fig. 3 are obtained using this initial state.

3. BCS initialization for phase III

Preparing the initial state for phase III requires the presence of a sharp domain wall and an order parameter of small magnitude. To obtain the domain wall, spins are first initialized in $|\downarrow\rangle_Z$ (i.e., in the unrotated spin space). An optical pumping beam selectively excites spins in a central region of radius r_d (chosen to be $r_d = R/2$) to $|\uparrow\rangle_Z$. A $\pi/2$ pulse about the $-Y$ axis then respectively converts the central and outer regions to domains of $|\uparrow\rangle_Z$ and $|\downarrow\rangle_Z$ spins (i.e., in the rotated spin space). To initialize a small order parameter, we assume that $w_{\mathrm{ODF}} = R/2$ and set the maximum pulse area to be $\Omega_{\mathrm{max}} T = 0.1\pi$, i.e., the spin rotation is through rather small angles. Furthermore, since the spins in the different domains start in opposite orientations, a partial cancelation occurs that further decreases the magnitude of the initial order parameter. Data shown in Fig. 2(c) are obtained using this initial state.

[1] R. A. Barankov and L. S. Levitov, Synchronization in the BCS Pairing Dynamics as a Critical Phenomenon, Phys. Rev. Lett. **96**, 230403 (2006).

[2] E. A. Yuzbashyan, M. Dzero, V. Gurarie, and M. S. Foster, Quantum quench phase diagrams of an s-wave BCS-BEC condensate, Phys. Rev. A **91**, 033628 (2015).

[3] Robert J. Lewis-Swan, Diego Barberena, Julia R. K. Cline, Dylan J. Young, James K. Thompson, and Ana Maria Rey, Cavity-QED Quantum Simulator of Dynamical Phases of a Bardeen-Cooper-Schrieffer Superconductor, Phys. Rev. Lett. **126**, 173601 (2021).

[4] Matthew S. Foster, Maxim Dzero, Victor Gurarie, and Emil A. Yuzbashyan, Quantum quench in a $p + ip$ superfluid: Winding numbers and topological states far from equilibrium, Phys. Rev. B **88**, 104511 (2013).

[5] C. A. Regal, C Ticknor, J. L. Bohn, and D. S. Jin, Tuning p-Wave Interactions in an Ultracold Fermi Gas of Atoms, Phys. Rev. Lett. **90**, 053201 (2003).

[6] C. H. Schunck, M. W. Zwierlein, C. A. Stan, S. M. F. Raupach, W. Ketterle, A. Simoni, E. Tiesinga, C. J. Williams, and P. S. Julienne, Feshbach resonances in fermionic ^{6}Li, Phys. Rev. A **71**, 045601 (2005).

[7] J. P. Gaebler, J. T. Stewart, J. L. Bohn, and D. S. Jin, p-Wave Feshbach Molecules, Phys. Rev. Lett. **98**, 200403 (2007).

[8] Kenneth Günter, Thilo Stöferle, Henning Moritz, Michael Köhl, and Tilman Esslinger, p-Wave Interactions in Low-Dimensional Fermionic Gases, Phys. Rev. Lett. **95**, 230401 (2005).

[9] Y.-J. Han, Y.-H. Chan, W. Yi, A. J. Daley, S. Diehl, P. Zoller, and L.-M. Duan, Stabilization of the p-Wave Superfluid State in an Optical Lattice, Phys. Rev. Lett. **103**, 070404 (2009).

[10] N. R. Cooper and G. V. Shlyapnikov, Stable Topological Superfluid Phase of Ultracold Polar Fermionic Molecules, Phys. Rev. Lett. **103**, 155302 (2009).

[11] A. K. Fedorov, S. I. Matveenko, V. I. Yudson, and G. V. Shlyapnikov, Novel p-wave superfluids of fermionic polar molecules, Sci. Rep. **6**, 27448 (2016).

[12] Matthew S. Foster, Victor Gurarie, Maxim Dzero, and Emil A. Yuzbashyan, Quench-Induced Floquet Topological p-Wave Superfluids, Phys. Rev. Lett. **113**, 076403 (2014).

[13] Kevin A. Gilmore, Matthew Affolter, Robert J. Lewis-Swan, Diego Barberena, Elena Jordan, Ana Maria Rey, and John J. Bollinger, Quantum-enhanced sensing of displacements and electric fields with two-dimensional trapped-ion crystals, Science **373**, 673 (2021).

[14] Martin Gärttner, Justin G Bohnet, Arghavan Safavi-Naini, Michael L Wall, John J Bollinger, and Ana Maria Rey, Measuring out-of-time-order correlations and multiple quantum spectra in a trapped-ion quantum magnet, Nat. Phys. **13**, 781 (2017).

[15] P. W. Anderson, Random-phase approximation in the theory of superconductivity, Phys. Rev. **112**, 1900 (1958).

[16] Athreya Shankar, Chen Tang, Matthew Affolter, Kevin Gilmore, Daniel H. E. Dubin, Scott Parker, Murray J. Holland, and John J. Bollinger, Broadening of the drumhead-mode spectrum due to in-plane thermal fluctuations of two-dimensional trapped ion crystals in a Penning trap, Phys. Rev. A **102**, 053106 (2020).

[17] We note that the form of the interaction in Eq. (1) is only valid for momenta with magnitude p such that $pd \ll 1$, where d is the range of the interaction potential. In practice, the finite number of fermions means that only momenta with $pd \ll 1$ are occupied and relevant during the dynamics. In the trapped-ion implementation we propose in this work, the ion crystal radius serves as a hard cutoff on the range of momenta involved.

[18] For each pair of fermions at $(+\mathbf{p}, -\mathbf{p})$, we can choose to define a spin according to Eqs. (3) either at $+\mathbf{p}$ or at $-\mathbf{p}$ to ensure that all spin operators are independent. Let $+\mathbf{p}$ $(-\mathbf{p})$ correspond to momenta with $p_y > 0$ $(p_y < 0)$. To uniformly cover the 2D momentum plane, when we convert from Eqs. (2)–(4), we choose half the total number of $(+\mathbf{p}, -\mathbf{p})$ pairs to map to spins at $+\mathbf{p}$ and the remaining half to map to spins at $-\mathbf{p}$. Thus, the summation over the indices $\mathbf{p}$, $\mathbf{q}$ in Eq. (4) is over half the number of values compared to Eq. (2). In Ref. [4], independent spin operators are ensured in a different manner by choosing to map to spins in a single half-plane, i.e., to spins at $+\mathbf{p}$ ($p_y > 0$ plane) only.

[19] J. Dukelsky, S. Pittel, and G. Sierra, Colloquium: Exactly solvable Richardson-Gaudin models for many-body quantum systems, Rev. Mod. Phys. **76**, 643 (2004).

[20] C.-C. Joseph Wang, Adam C. Keith, and J. K. Freericks, Phonon-mediated quantum spin simulator employing a planar ionic crystal in a Penning trap, Phys. Rev. A **87**, 013422 (2013).

[21] D. F. James and J Jerke, Effective Hamiltonian theory and its applications in quantum information, Can. J. Phys. **85**, 625 (2007).

[22] Joseph W. Britton, Brian C. Sawyer, Adam C. Keith, C. C Joseph Wang, James K. Freericks, Hermann Uys, Michael J. Biercuk, and John J. Bollinger, Engineered two-dimensional Ising interactions in a trapped-ion quantum simulator with hundreds of spins, Nature **484**, 489 (2012).

[23] Wenchao Ge, Brian C. Sawyer, Joseph W. Britton, Kurt Jacobs, John J. Bollinger, and Michael Foss-Feig, Trapped Ion Quantum Information Processing with Squeezed Phonons, Phys. Rev. Lett. **122**, 030501 (2019).

[24] J. Schachenmayer, A. Pikovski, and A. M. Rey, Many-Body Quantum Spin Dynamics with Monte Carlo Trajectories on a Discrete Phase Space, Phys. Rev. X **5**, 011022 (2015).

[25] Mohit Randeria and Edward Taylor, Crossover from Bardeen-Cooper-Schrieffer to Bose-Einstein condensation and the unitary Fermi gas, Annu. Rev. Condens. Matter Phys. **5**, 209 (2014).

[26] Lukas Schwarz, Benedikt Fauseweh, and Dirk Manske, Momentum-resolved analysis of condensate dynamic and Higgs oscillations in quenched superconductors with time-resolved ARPES, Phys. Rev. B **101**, 224510 (2020).

[27] Jan von Delft, Superconductivity in ultrasmall metallic grains, Ann. Phys. **10**, 219 (2001).

[28] Yunxiang Liao and Matthew S. Foster, Spectroscopic probes of isolated nonequilibrium quantum matter: Quantum quenches, Floquet states, and distribution functions, Phys. Rev. A **92**, 053620 (2015).

[29] Sankalp Gaur, Victor Gurarie, and Emil A. Yuzbashyan, Singularities in the Loschmidt echo of quenched topological superconductors, (2022),.

[30] Shane P. Kelly, James K. Thompson, Ana Maria Rey, and Jamir Marino, Resonant light enhances phase coherence in a cavity QED simulator of fermionic superfluidity, (2022), arXiv preprint ArXiv:2202.05851.

[31] Ryusuke Matsunaga, Naoto Tsuji, Hiroyuki Fujita, Arata Sugioka, Kazumasa Makise, Yoshinori Uzawa, Hirotaka Terai, Zhen Wang, Hideo Aoki, and Ryo Shimano, Light-induced collective pseudospin precession resonating with Higgs mode in a superconductor, Science **345**, 1145 (2014).

[32] Ryusuke Matsunaga, Yuki I. Hamada, Kazumasa Makise, Yoshinori Uzawa, Hirotaka Terai, Zhen Wang, and Ryo Shimano, Higgs Amplitude Mode in the BCS Superconductors $Nb_{1-x}Ti_xN$ Induced by Terahertz Pulse Excitation, Phys. Rev. Lett. **111**, 057002 (2013).

[33] Ryusuke Matsunaga, Naoto Tsuji, Kazumasa Makise, Hirotaka Terai, Hideo Aoki, and Ryo Shimano, Polarization-resolved terahertz third-harmonic generation in a single-crystal superconductor NbN: Dominance of the Higgs mode beyond the BCS approximation, Phys. Rev. B **96**, 020505 (2017).

[34] M. Mitrano, A. Cantaluppi, D. Nicoletti, S. Kaiser, A. Perucchi, S. Lupi, P. Di Pietro, D. Pontiroli, M. Riccò, S. R. Clark, D. Jaksch, and A. Cavalleri, Possible light-induced superconductivity in K_3C_{60} at high temperature, Nature **530**, 461 (2016).

[35] R. Mankowsky, A. Subedi, M. Först, S. O. Mariager, M. Chollet, H. T. Lemke, J. S. Robinson, J. M. Glownia, M. P. Minitti, A. Frano, M. Fechner, N. A. Spaldin, T. Loew, B. Keimer, A. Georges, and A. Cavalleri, Nonlinear lattice dynamics as a basis for enhanced superconductivity in $YBa_2Cu_3O_{6.5}$, Nature **516**, 71 (2014).

[36] Kazuki Isoyama, Naotaka Yoshikawa, Kota Katsumi, Jeremy Wong, Naoki Shikama, Yuki Sakishita, Fuyuki Nabeshima, Atsutaka Maeda, and Ryo Shimano, Light-induced enhancement of superconductivity in iron-based superconductor $FeSe_{0.5}Te_{0.5}$, Commun. Phys. **4**, 160 (2021).

[37] M. A. Sentef, M. Ruggenthaler, and A. Rubio, Cavity quantum-electrodynamical polaritonically enhanced electron-phonon coupling and its influence on superconductivity, Sci. Adv. **4**, eaau6969 (2018).

[38] Frank Schlawin and Dieter Jaksch, Cavity-Mediated Unconventional Pairing in Ultracold Fermionic Atoms, Phys. Rev. Lett. **123**, 133601 (2019).

[39] Jonathan B. Curtis, Zachary M. Raines, Andrew A. Allocca, Mohammad Hafezi, and Victor M. Galitski, Cavity Quantum Eliashberg Enhancement of Superconductivity, Phys. Rev. Lett. **122**, 167002 (2019).

[40] Anoop Thomas, Eloïse Devaux, Kalaivanan Nagarajan, Thibault Chervy, Marcus Seidel, David Hagenmüller, Stefan Schütz, Johannes Schachenmayer, Cyriaque Genet, Guido Pupillo, and Thomas W. Ebbesen, Exploring superconductivity under strong coupling with the vacuum electromagnetic field, (2019), ArXiv:1911.01459.

[41] Ahana Chakraborty and Francesco Piazza, Long-Range Photon Fluctuations Enhance Photon-Mediated Electron Pairing and Superconductivity, Phys. Rev. Lett. **127**, 177002 (2021).

[42] S. C. Burd, R. Srinivas, H. M. Knaack, W. Ge, A. C. Wilson, D. J. Wineland, D. Leibfried, J. J. Bollinger, D. T. C. Allcock, and D. H. Slichter, Quantum amplification of boson-mediated interactions, Nat. Phys. **17**, 898 (2021).

[43] M. Dzero, E. A. Yuzbashyan, and B. L. Altshuler, Cooper pair turbulence in atomic Fermi gases, EPL (Europhys. Lett.) **85**, 20004 (2009).

[44] Mark H. Fischer, Titus Neupert, Christian Platt, Andreas P. Schnyder, Werner Hanke, Jun Goryo, Ronny Thomale, and Manfred Sigrist, Chiral *d*-wave superconductivity in SrPtAs, Phys. Rev. B **89**, 020509 (2014).

[45] Anthony M. Polloreno, Ana Maria Rey, and John J. Bollinger, Individual qubit addressing of rotating ion crystals in a Penning trap, (2022),.

[46] Liang Jiang, Takuya Kitagawa, Jason Alicea, A. R. Akhmerov, David Pekker, Gil Refael, J. Ignacio Cirac, Eugene Demler, Mikhail D. Lukin, and Peter Zoller, Majorana Fermions in Equilibrium and in Driven Cold-Atom Quantum Wires, Phys. Rev. Lett. **106**, 220402 (2011).

[47] Christina V. Kraus, Marcello Dalmonte, Mikhail A. Baranov, Andreas M. Läuchli, and P. Zoller, Majorana Edge States in Atomic Wires Coupled by Pair Hopping, Phys. Rev. Lett. **111**, 173004 (2013).

[48] Christina Psaroudaki and Christos Panagopoulos, Skyrmion Qubits: A New Class of Quantum Logic Elements Based on Nanoscale Magnetization, Phys. Rev. Lett. **127**, 067201 (2021).

[49] We discuss this approximation in more detail in Appendix B.

[50] Justin G. Bohnet, Brian C. Sawyer, Joseph W. Britton, Michael L. Wall, Ana Maria Rey, Michael Foss-Feig, and John J. Bollinger, Quantum spin dynamics and entanglement generation with hundreds of trapped ions, Science **352**, 1297 (2016).

[51] H. Uys, M. J. Biercuk, A. P. VanDevender, C. Ospelkaus, D. Meiser, R. Ozeri, and J. J. Bollinger, Decoherence due to Elastic Rayleigh Scattering, Phys. Rev. Lett. **105**, 200401 (2010).

[52] Allison Carter, private communication (to be published).

[53] Jan Müller, *Magnetic Skyrmions and Topological Domain Walls*, Ph.D. thesis, Universität zu Köln (2018).